Title: A connectional hub in the rostral anterior cingulate cortex links areas of emotion and cognitive control.

Authors: Wei Tang[1], Saad Jbabdi[2], Ziyi Zhu[3], Michiel Cottaar[2], Giorgia Grisot[4], Julia Lehman[3], Anastasia Yendiki[4], and Suzanne N. Haber*[1,3].

Affiliations: [1]McLean Hospital & Harvard Medical School, Belmont, MA 02478, USA; [2]Centre for Functional MRI of the Brain, Department of Clinical Neurology, University of Oxford, Oxford, UK; [3]Department of Pharmacology and Physiology, University of Rochester School of Medicine & Dentistry, Rochester, NY 14642, USA; [4]Athinoula A. Martinos Center for Biomedical Imaging, Massachusetts General Hospital & Harvard Medical School, Charlestown, MA 02129, USA

Contact Information:

*Suzanne Haber, Corresponding Author and Lead Contact

Department of Pharmacology and Physiology

University of Rochester Medical Center

601 Elmwood Avenue,

Rochester, NY 14642

Telephone: (585) 275-4538

FAX: (585) 273-2652

E-mail: suzanne_haber@urmc.rochester.edu

Abstract

We investigated afferent inputs from all areas in the frontal cortex (FC) to different subregions in the rostral anterior cingulate cortex (rACC). Using retrograde tracing in macaque monkeys, we quantified projection strength by counting retrogradely labeled cells in each FC area. The projection from different FC regions varied across injection sites in strength, following different spatial patterns. Importantly, a site at the rostral end of the cingulate sulcus stood out as having strong inputs from many areas in diverse FC regions. Moreover, it was at the integrative conjunction of three projection trends across sites. This site marks a connectional hub inside the rACC that integrates FC inputs across functional modalities. Tractography with monkey diffusion magnetic resonance imaging (dMRI) located a similar hub region comparable to the tracing result. Applying the same tractography method to human dMRI data, we demonstrated that a similar hub can be located in the human rACC.

Introduction

The anterior cingulate cortex (ACC) is composed of multiple regions that support a wide range of functions (emotion, motivation, higher cognition, and motor control), and thus, is in a position to use value-related information to help regulate flexibility, adaptation and top-down control (Etkin, Buchel, & Gross, 2015; Kolling et al., 2016; Shenhav, Cohen, & Botvinick, 2016). This functionally heterogeneous region is anatomically divided into the subgenual ACC (sACC), the rostral ACC (rACC), and the dorsal ACC (dACC) (Morecraft et al., 2012; Morecraft & Tanji, 2009; Ongur & Price, 2000). The sACC is connected to the motivation network consisting of the orbitofrontal cortex (OFC) and the amygdala. It is involved in visceral and emotional functions, an important mediator of motivation, and is critical for determining value (Camille, Griffiths, Vo, Fellows, & Kable, 2011; Jocham, Hunt, Near, & Behrens, 2012; Kolling et al., 2016). The rACC is tightly linked with both the sACC and the dorsolateral and ventrolateral prefrontal cortex (dlPFC and vlPFC), and is associated with cognitive control and choice of action (Jiang, Beck, Heller, & Egner, 2015; Kolling, Scholl, Chekroud, Trier, & Rushworth, 2018). Caudally, the dACC is connected with the action network consisting of motor control areas, including frontal eye fields (FEF) and premotor areas (Morecraft et al., 2012; Ongur & Price, 2000). The dACC is associated with motor planning and action execution (Caruana et al., 2018; Picard & Strick, 1996). Importantly, the connections of these divisions are a continuum and there are no specific borders between the ACC subdivisions (Morecraft et al., 2012).

The rACC sits at the connectional intersection of the motivation and action control networks. In regard to the ACC functions, the rACC is in an important position in the transition from valuation to choice to action. An important question is how the transitions occur within the rACC. One

68 possibility is that information processing changes sequentially across subregions within the rACC,
69 from valuation in regions close to the sACC, to cognition at the center of the rACC, and then to
70 action in regions close to the dACC (Kable & Glimcher, 2009; Rangel & Hare, 2010; Shadlen,
71 Kiani, Hanks, & Churchland, 2008). Alternatively, different functional processing may be
72 integrated at a hub (Cisek, 2012; Hunt, Woolrich, Rushworth, & Behrens, 2013; Kolling, Behrens,
73 Mars, & Rushworth, 2012; Lee, Shimojo, & O'Doherty, 2014; Rushworth, Kolling, Sallet, & Mars,
74 2012). Network science defines a hub as a node of a network that has a significantly larger number
75 of links compared to other nodes in the network. In brain network analyses, the hub regions that
76 have disproportionally numerous connections to other regions are considered central for
77 integrating information from functionally diverse regions (van den Heuvel & Sporns, 2013). In
78 this regard, the entire rACC can be considered a hub (Buckner et al., 2009). However, as the rACC
79 is a large area, we sought to determine whether there is a specific region within it that is uniquely
80 positioned to integrate signals across several functional domains.
81
82 To determine whether a hub region exists in the rACC, we systematically placed tracer injections
83 along the rACC in nonhuman primates (NHP), and quantified the input strength and patterns from
84 the frontal cortex (FC) to each injection site. As expected, projections from the vmPFC were
85 concentrated in the ventral rACC and those from motor control areas were found more dorsally
86 and caudally. Projections from the vlPFC, the dlPFC, the dmPFC and the OFC varied across sites.
87 However, one site showed uniquely numerous and diverse connections with the FC, suggesting a
88 hub region at this site. To test whether a similar connectivity pattern and the location of a hub
89 could be identified in the human rACC using dMRI, we first investigated the accuracy of dMRI in
90 detecting connectivity convergence using high resolution dMRI in NHPs. We seeded each frontal

area and, consistent with the tracing results, probabilistic streamlines converged in a similar location as the hub within the rACC. We then seeded each frontal area in a dMRI dataset from the Human Connectome Project (HCP). As in the NHP results, the streamlines converged in a similar rACC location.

Materials and Methods

Overview. Bidirectional tracer injections were placed systematically throughout the rACC. FC was divided based on cytoarchitectonics into areas (Pandya & Seltzer, 1982; Paxinos, Huang, & Toga, 2000; Preuss & Goldman-Rakic, 1991; Vogt, 1993a; Brent A. Vogt, 2009) and retrogradely labeled cells were quantified using StereoInvestigator. To normalize for comparison across cases (variability in uptake and transport), we calculated the percentage of total labeled cells that projected from each area to each injection site. These percent scores were independent from the size of each area. The areas were further pooled into major FC regions according to their associated functions. Using the percent scores as the measurement for input strength, projection gradient across injection sites was analyzed for each FC region. Guided by the tracing results, probabilistic tractography was conducted on the NHP and human dMRI. Cortical areas were used as seed masks and the rACC as the target mask. The connectivity strength was determined by the number of streamlines between each target voxel and an FC area, divided by the total number of streamlines from that area to all rACC voxels. A convergent-connectivity value was calculated for each rACC voxel as the sum of connectivity strength weighted by the number of areas with non-zero streamlines. We identified voxels with the highest convergent-connectivity value for each individual subject and compared their locations to the hub region found in tract tracing.

Anatomical tracing experiments. All experiments were performed in accordance with the Institute of Laboratory Animal Resources Guide for the Care and Use of Laboratory Animals and approved by the University Committee on Animal Resources at University of Rochester. Animals were adult male monkeys (*Macaca mulatta* and *Macaca fascicularis*). Bidirectional tracers were injected into the rACC. Details of the surgical and histological procedures have been described previously (Haber, Kim, Mailly, & Calzavara, 2006; Safadi et al., 2018). Monkeys were first tranquilized by intramuscular injection of ketamine (10 mg/kg) and then maintained anesthetized via 1%–3% isoflurane in 100% oxygen. Temperature, heart rate, and respiration were monitored throughout the surgery. Pre-surgery structural MR images were used to locate the stereotaxic coordinates for the injection sites. Monkeys were placed in a David Kopf Instruments stereotax, a craniotomy (2–3 cm) was made over the region of interest, and small dural incisions were made at injection sites. Bidirectional tracers (40–50 µl, 10% in 0.1 mol phosphate buffer (PB), pH 7.4; Invitrogen) were pressure injected over 10 min using a 0.5 µl Hamilton syringe, separate for each case. Tracers used for the present study were Lucifer Yellow (LY), Fluororuby (FR), or Fluorescein (FS) conjugated to dextran amine (Invitrogen). After each injection, the syringe remained *in situ* for 20–30 min.

After a survival period of 12–14 days, monkeys were again deeply anesthetized and perfused with saline, followed by a 4% paraformaldehyde/1.5% sucrose solution in 0.1 mol PB, pH 7.4. Brains were postfixed overnight and cryoprotected in increasing gradients of sucrose (10, 20, and 30%; (Haber et al., 2006)). Brains were removed and shipped to the Martinos Center for Biomedical Imaging. Diffusion MRI data was collected with the brains submerged in Fomblin solution to eliminate susceptibility artifacts at air-tissue interfaces and background signal (see *dMRI data collection and analysis* for imaging protocols). After imaging, the brains were shipped back to University of Rochester Medical Center for histological processing. Serial sections of 50 µm were

cut on a freezing microtome, and one series with sections 1.2 mm-apart was processed for subsequent retrograde tracing. The serial sections were processed free-floating for immunocytochemistry. Tissue was incubated in primary anti-LY (1:3000 dilution; Invitrogen), anti-FS (1:1000; Invitrogen), or anti-FR (1:1000; Invitrogen) in 10% NGS and 0.3% Triton X-100 (Sigma-Aldrich) in PB for 4 nights at 4°C. After extensive rinsing, the tissue was incubated in biotinylated secondary antibody followed by incubation with the avidin-biotin complex solution (Vectastain ABC kit, Vector Laboratories). Immunoreactivity was visualized using standard DAB procedures. Staining was intensified by incubating the tissue for 5–15 s in a solution of 0.05% DAB tetrahydrochloride, 0.025% cobalt chloride, 0.02% nickel ammonium sulfate, and 0.01% H_2O_2. Sections were mounted onto gel-coated slides, dehydrated, defatted in xylene, and coverslipped with Permount. In cases in which more than one tracer was injected into a single animal, adjacent sections were processed for each antibody reaction.

Analysis: strength of inputs and defining the hub. Seven out of sixteen injection sites were selected for analysis based on the following criteria (Fig. 1): 1. Location of the injection site along the rACC; 2. lack of tracers leaking into adjacent cortical regions or into the white matter; 3. outstanding transport; and 4. low background. Two cases were in the same position, however, one particularly large, and served as a control for size. This case demonstrated that the number and strength of projection to a site was not dominated by the injection size, but rather its position. To evaluate the strength of the different FC inputs to each injection site, we divided the FC into 27 areas based on the atlas by Paxinos et al. (2000), in conjunction with detailed anatomical descriptions (Pandya & Seltzer, 1982; Preuss & Goldman-Rakic, 1991; B. A. Vogt, 2009b; Vogt, 1993b). Labeled cells were quantified throughout the prefrontal cortex (PFC) and the premotor

159 cortex using StereoInvestigator software (MicroBrightField) as previously described (Choi,
160 Tanimura, Vage, Yates, & Haber, 2016). To compare the input pattern across injection sites, the
161 percent input to each site was calculated based on the number of labeled cells in each FC area
162 projecting to a given site, divided by the total number of labeled cells across all FC areas projecting
163 to the same site. Areas were then ordered based on their percent scores. The number of areas whose
164 cell counts added up to 50% and 75% of total input was calculated for each site. To determine
165 whether the inputs were distributed evenly across areas or highly concentrated in a few areas, an
166 entropy score was calculated to compare the input pattern to a uniform distribution:

167 $$H = -\sum_{i=1}^{27} c_i \log(c_i) \quad (1)$$

168 where c_i is the percent cell count for the i-th area, and log() is the natural logarithm function
169 (Conrad, 2004). The hub was characterized by a high number of areas contributing to 50% and 75%
170 of total inputs. Additionally, the hub was expected to have a high entropy score that indicates
171 evenly distributed inputs across areas.
172
173 *Definition of commonly referred regions*. To determine whether inputs to each site show spatial
174 regularity in their cortical origin, FC areas were grouped into regions commonly used in the
175 terminology of functional studies (see e.g. (Clark, Boutros, & Mendez, 2010)). These included:
176 frontal pole (FP, area 10), vmPFC (areas 14M, 25), OFC (areas 14O, 11, 13, OPAl, OPro), vlPFC
177 (areas 47, 47O, 44, 45), dlPFC (areas 9, 46, 9/46), dmPFC (areas 9/32, 9M), frontal eye field (FEF,
178 area 8) and premotor cortex (areas 6, ProM, 6/32). We note that in many functional imaging studies
179 in human, the demarcation of vmPFC includes the medial part of Broadmann Area 10. However,
180 area 10 in both NHPs and humans has a dorsal and a lateral part that covers the entire polar region.

181 To maintain cytoarchitectonic consistency in spatial demarcation, we separated area 10 from
182 vmPFC entirely and designated it as FP.
183
184 *dMRI data collection and analysis*. The dMRI data collection and preprocessing was previously
185 described in Safadi et al. (2018). The NHP dMRI data was collected from 7 animals in a small-
186 bore 4.7T Bruker BioSpin MRI system, with gradient internal diameter of 116 mm, maximum
187 gradient strength 480 mT/m, and birdcage volume RF coil internal diameter of 72 mm. A 3D echo-
188 planar imaging (EPI) sequence was used for dMRI with TR = 750 ms, TE = 43 ms, δ = 15 ms, Δ
189 = 19ms, b_{max} = 40,000 s/mm^2, 514 gradient directions, matrix size 96 × 96 × 112, and 0.7 mm
190 isotropic resolution. The human dMRI data used 35 healthy subjects, publicly available as part of
191 the MGH-USC Human Connectome Project (HCP) (Fan et al., 2016). Both the NHP and human
192 data were preprocessed using FSL 5.0.9 (Jenkinson, Beckmann, Behrens, Woolrich, & Smith,
193 2012). Artifacts of head movements and distortions by eddy currents were corrected(Andersson &
194 Sotiropoulos, 2016). A crossing fiber model (bedpostx)(Behrens, Berg, Jbabdi, Rushworth, &
195 Woolrich, 2007) was fit to each voxel to estimate the distribution of fiber orientations, which were
196 subsequently used in the probabilistic tractography.
197
198 Following preprocessing, probabilistic tractography (Behrens et al., 2007) was performed in each
199 individual's diffusion space, and the results were transformed to a template for comparison across
200 subjects. Parcellation of the FC areas for NHP followed the same atlas used for tract tracing
201 (Paxinos et al., 2000). Each FC area was used as a seed, while ACC areas 32 and 24 were combined
202 and used as the target. Twenty-seven seed masks were created correspondent to the 27 FC areas
203 used in the tracing analysis. To generate seed and target masks, areal masks from a template brain

(Calabrese et al., 2015) were transformed to each individual's diffusion space via nonlinear registration (Klein, Staring, Murphy, Viergever, & Pluim, 2010). Each mask covers 0.14 mm thickness (2 voxels) of white matter at the gray-white matter boundary (Fig. 7B). Anatomical parcellation of the human cortex was hand drawn on a surface-based template (*fsaverage* by FreeSurfer 4.5, Fig. 8A). The parcellation followed Petrides et al. (2012), which was developed to maximize architectonic correspondence between human and NHP prefrontal areas (see Discussion on the cross-species homologies). Twenty-five hand-drawn masks were transformed from the *fsaverage* space to each individual's diffusion space with nonlinear registration provided by FreeSurfer. The FC areas were used as seeds, and areas 32 and 24 were combined and used as the target. Each mask covers 3 mm thickness (2 voxels) of white matter at the gray-white matter boundary.

FSL was used for probabilistic tractography for both NHP and human. Tractography was performed from each seed mask to the ipsilateral target mask. At each voxel, a sample was drawn from the orientation distribution of the anisotropic compartment with the closest orientation to the previously visited voxel (Behrens et al., 2007). To exclude indirect pathways through subcortical structures, the thalamus, the striatum and the amygdala were used as exclusion masks. To measure the connectivity strength between each seed mask and each target voxel, the number of streamlines arriving at the target voxel was divided by the total number of streamlines generated from the seed mask. The convergent-connectivity value was defined as the sum of areas with non-zero streamlines multiplied by the connectivity strength. The final results from all individuals were displayed on a template brain via linear registration (FA image of the template by Calabrese et al., 2015 for NHP, T1-weighted image of the MNI152 template for human).

Results

Overview. Injection sites were labeled 1-6 based on the spatial order of their locations (Fig. 1). Sites 1–3 were in area 32 and labeled from caudal to rostral respectively. Site 4 was in the transition zone between areas 32 and 24. Sites 5 and 6 were in area 24. Sites 4-6 were labeled from rostral to caudal. The additional large injection was in area 24 and overlapped with site 5, but, extended beyond the borders of site 5. This case served as a control for the variability of injection size. Retrogradely labeled FC cells were quantified in each case for each area. The projection strength from each cortical area was calculated based on the percent of total labeled cells. The sites differed with respect to projection strength from various FC areas to each site. The results demonstrated 3 projection patterns across sites: a decrease in the input strength to sites 1-6 from the FP and the vmPFC; an increase in the input strength to sites 1-6 from the FEF and the premotor cortex; a non-monotonic gradient centered on site 4 with the input strength from the dlPFC, the dmPFC and the vlPFC increasing to sites 1-4 and decreasing to sites 4-6. Taken together the results show that site 4 receives inputs from the greatest number of FC areas. It also contains the most regionally diverse inputs compared to the other sites. Finally, consistent with the tracing results, dMRI tractography in NHP and human showed convergent probabilistic tracts from the FC to an rACC region in close proximity to site 4.

Projection patterns from the FC areas to the rACC. Not all FC regions project equally to the rACC. Overall, retrogradely labeled cells in cases 1-3 were primarily located in more rostral regions of the FC, while those in cases 4-6 were primarily in more caudal regions (Fig. 2). Case 1 showed high concentration of labeled cells at the rostral pole of the medial PFC. However, at more caudal levels, the concentration of labeled cells was located primarily ventrally, with few labeled cells in

areas 9 and 9/32. In addition, there were clusters of labeled cells located in a caudal OFC area OPro. Similarly, in cases 2 and 3, labeled cells were concentrated rostrally in the FP and the vmPFC regions. However, some clusters with a few labeled cells were also located more dorsally in area 9L and caudally in the lateral OFC. In contrast for case 1, additional labeled cells were found in the vlPFC (areas 47L and 47O). Case 4 showed a diverse pattern to the distribution of labeled cells, with a clear increase of dense clusters of labeled cells located in dorsal regions. At the most rostral level, labeled cells were concentrated in the FP. At more caudal levels, labeled cells were extensively distributed in the dlPFC, the vlPFC, ventromedial OFC and the vmPFC. An additional cluster of labeled cells was also found in area OPro. Case 5 resulted in labeled cells concentrated ventrally, primarily in the caudal part of orbital and medial regions, although scattered clusters of labeled cells were also located rostrally in the FP and dorsally in area 9. Finally, labeled cells in case 6 were primarily distributed in caudal dorsal regions, in area 8 and the premotor cortex. Only very few labeled cells were found in ventral or rostral regions.

An essential property of network hubs is their high degree of connections. To measure the degree of connection of each site, we identified the number of areas that contributed to 50% and 75% of total inputs. This number varied extensively across sites (Fig. 3). At site 1, only two areas, 25 and 10M accounted for 50% of the total inputs. Inputs from areas 10L and OPro accounted for an additional 25%, for a total of 4 areas comprising 75% of all inputs to site 1. Similarly, two areas, 10L and 10M contributed 50% of total inputs to site 2, and two areas 25 and 46 accounted for an additional 25%, for a total of 4 areas comprising 75% of all inputs to site 2. At site 3, three areas 25, 46 and 47O contributed 50% of the total inputs, with three additional areas 9L, 10L and 11 (the additional 25%) for a total of 6 areas comprising 75% of all inputs to site 3. In contrast to sites

1-3, site 4 received 50% of the total inputs from five FC areas 9L, 47O, 9M, OPro and 46. Five areas, 9/32, 14O, 14M, 8B and 9/46D, contributed the additional 25%, for a total of 10 areas comprising 75% of all inputs to site 4. More consistent with sites 1-2, site 5 received 50% of its inputs from only two areas, OPro and 47O. Four areas, 13, 10M, 25 and 9L contributed the remaining 25%, for a total of 6 areas comprising 75% of all inputs to site 5. The control site was large and had a higher number of labeled cells than all the other sites (Fig. S1A). Despite that, it showed a similar distribution of major input areas to that of site 5. The control site received 50% of its inputs from two areas, 13 and 47O. Three areas, OPAl, 47L and 46 contributed the remaining 25%, for a total of 5 areas comprising 75% of all inputs (Fig. S1B). Finally, four areas, 6L, 6/32, 9/46V and 8B, contributed 50% of total inputs to site 6. Five areas, 6M, 8A, ProM and 8/32 contributed an additional 25%, for a total of 8 areas comprising 75% of all inputs to site 6. In summary, the number of areas accounting for 50% and 75% of total inputs varied across sites (Table 2). Importantly, this was not a function of the differential size of the areas (Fig. S1C). The curves generated by calculating the number of areas contributing 50% of the total inputs to each site illustrate the relatively limited number of input to sites 1-3 and 5 compared to sites 4 and 6 (Figs. 3 & 4A). The entropy measure of cell counts across areas to verify that the difference of cell distribution across sites was not due to an arbitrary percentage cutoff. Consistent with the area counts in Fig. 4A, the entropy score was the lowest at sites 1 and 2, and the highest at site 4 and site 6 (Fig. 4B).

Projection patterns from cortical regions to the rACC. FC areas were grouped into commonly referred FC regions. These included: frontal pole (FP, area 10) and vmPFC (areas 14M, 25), OFC (areas 14O, 11, 13, OPAl, OPro), vlPFC (areas 47L, 47O, 44, 45), dlPFC (areas 9, 46, 9/46),

296 dmPFC (areas 9/32, 9M), frontal eye field-FEF (area 8), and premotor cortex (areas 6, ProM, 6/32).
297 At each site, we identified the FC regions contributing 50% and 75% inputs (Fig. 5). FP and
298 vmPFC contributed 50% of the total inputs to site 1. The next 25% were from FP and OFC, for a
299 total of 3 regions. At site 2, only FP contributed 50% of the inputs. Inputs from vmPFC and dlPFC
300 comprised the next 25% for a total of 3 regions. vmPFC, vlPFC and dlPFC contributed 50% inputs
301 to site 3, and OFC and FP the next 25% for a total of 5 regions. OFC, vlPFC, dmPFC and dlPFC
302 contributed 50% of the total inputs to site 4. The next 25% were from vmPFC, OFC, dlPFC and
303 FEF, for a total of 8 regions. Inputs from OFC and vlPFC comprised 50% of the inputs to sites 5.
304 The next 25% were from FP, vmPFC, OFC, and dlPFC, for a total of 5 regions contributing to 75%
305 of all the inputs to site 5. Finally, at site 6, both the 50% and 75% inputs were contributed by 3
306 regions: premotor cortex, FEF and dlPFC. In summary, sites 1, 2 and 5 had the most limited
307 regional input, and site 4 had the most diverse regional input.
308
309 *Projection trends from cortical regions to the rACC.* Using the mean percent score for the
310 projection strength from each cortical region to each site, we identified three modes of cortical
311 projection patterns to the rACC (Fig. 6). There were two monotonic trends across all sites, one
312 related to the FP and vmPFC projections, the other the premotor and FEF projections. The third
313 mode was a nonmonotonic gradient with a single peak at site 4, related to the dlPFC, vlPFC, and
314 dmPFC projections. In the first trend, vmPFC and FP contributed to more than 15% of inputs to
315 sites 1 and 2, ~10% to site 3, just under 5% to sites 4 and 5, and close to 0% to site 6 (Fig. 6A).
316 The between-site difference was statistically significant (Kruskal-Wallis $H = 10.48$, $p < 0.02$). This
317 trend indicates a decrease in projection strength of vmPFC and FP along a gradient from site 1 to
318 6. In contrast, the second trend demonstrates an increase of projection strength from site 1 to 6 of

319 inputs from premotor cortex and FEF. These regions projected strongly to site 6, but weakly to the
320 other sites. Indeed, the average contribution of an area in these regions was less than 1% to the
321 inputs to sites 1-3, ~2% to sites 4 and 5, and more than 5% to site 6 (Fig. 6B). The between-site
322 difference was also statistically significant (Kruskal-Wallis $H = 35.46$, $p < 1\times10^{-5}$). Unlike
323 projections from FP and vmPFC, this trend is less evenly distributed along a gradient from site 1-
324 6, as the projections are concentrated in site 6. The final projection pattern is a single-peak
325 nonmonotonic gradient centered at site 4. The average input strength from dlPFC, vlPFC and
326 dmPFC increases from site 1 (~1%) to site 4 (> 5%) and then decreases from site 4 to site 6 (~2%).
327 The change across sites is more gradual than that in the 2 monotonic trends. The between-site
328 difference was statistically significant (Kruskal-Wallis $H = 20.18$, $p < 0.01$). Interestingly, OFC
329 areas did not show a trend across the rACC (Fig. 6D). Rather, the OFC projection was strongest
330 to site 5 (8%), 1 (5%), and 4 (4%) and less so to sites 2 (2%) and 6 (1%).
331
332 *Summary.* FC inputs to 6 sites in the rACC varied with respect to strength and regions of origin
333 (Table 2). Site 1 & 2 receive the strongest (50%) inputs from 2 areas (vmPFC and FP); site 3
334 receives the strongest inputs from 3 areas (vmPFC, vlPFC and dlPFC); site 4 receives the strongest
335 inputs from 5 areas (OFC, vlPFC, dmPFC and dlPFC); site 5 receives the strongest inputs from 2
336 areas (OFC and vlPFC); and site 6 receives the strongest inputs from 4 areas (dlPFC, FEF and
337 premotor cortex). Importantly, site 4 stands out as having the highest number of areas that
338 contributed 50% and 75% of inputs to it. Site 4 also had the most diverse cortical inputs. Across
339 sites, the projection strength of different regions formed 3 spatial patterns: vmPFC and FP showed
340 increasing projection strength from site 1 to 6; FEF and premotor cortex showed decreasing

341 projection strength from site 1 to 6. The third pattern was a nonmonotonic gradient formed by
342 projections from dlPFC, dmPFC and vlPFC, with a single peak centered at site 4.
343
344 *Convergent probabilistic tracts from the FC to the rACC in dMRI.* The FC of NHP dMRI images
345 was parcellated into 27 areas that corresponded to the 27 areas used in the tracing analysis (Fig.
346 7A). Each area was used as a seed mask. Areas 24 and 32 were combined as the target mask.
347 Probabilistic streamlines from the different seeds terminated in partially overlapping regions in the
348 target mask. Each streamline was a probabilistic estimation of the path that connects a seed voxel
349 and a voxel in the ACC. As an example, Fig. 7B shows two seed masks from areas 11 and 46, and
350 Fig. 7C illustrates the voxels where streamlines from the two seed masks terminate in the ACC in
351 one monkey. A subgroup of the streamlines from both areas targeted the same voxels (shown in
352 orange in Fig. 7C). We identified the location of highest convergence, i.e. the voxel receiving
353 streamlines from the most number of seeds. A convergent-connectivity value was calculated for
354 each voxel in the target mask, approximating the number of areas with high density of streamlines
355 to that voxel. Consistently across 7 monkeys, the highest convergence-connectivity value found
356 across all animals was located at the rostral edge of the cingulate sulcus (Fig. 7D). This is in a
357 similar location as site 4 in the tracing experiments (see Fig. 1A). There was some individual
358 variability on the dorsal-ventral axis. In 3 animals, the highest convergent-connectivity value was
359 just dorsal to the cingulate sulcus and in 4 animals it was just ventral to the sulcus.
360
361 We applied the same tractography method to human dMRI data. The human FC was parcellated
362 into 25 areas following Petrides and Pandya (1994). This anatomical division was developed to
363 maximize architectonic correspondence between human and NHP frontal areas (OPro and OPAl

were not clearly defined in the human parcellation by Petrides and Pandya (1994), and were thus not included in our human dMRI analysis). Similar to the NHP analysis, areas 32 and 24 were combined as the ACC target mask. Probabilistic streamlines were generated from each seed to the target. A convergent-connectivity value was calculated for each voxel in the target mask. The results demonstrated that, as in the NHP results, streamlines in each subject converged in the rACC. The highest convergent-connectivity value was consistently located in the rostral part of the rACC for all subjects (Fig. 8). The geometric center of the individual results was at the genu of the cingulate gyrus. This region was spatially approximate to site 4 in the NHP tracing study. Despite the morphological difference of cingulate sulcus between human and NHP, the geometric center of the results in Fig. 8 was at the rostral edge of the human cingulate sulcus, based on the Mai human atlas (Mai, Paxinos, & Voss, 2008). Interestingly, as in the NHP data, there was little individual variance in the rostrocaudal location of the convergence. However, similar to the NHP results, there was some individual variation in the dorsal-ventral axis. Importantly, as seen in NHP data, about half of the subjects had the voxel of highest convergence above the genu, and the other half below the genu.

Discussion

In this study we mapped out the FC inputs to different subregions within the rACC: Site 1-3 were in area 32. Site 1 was the closest to the sACC. It receives the strongest inputs from the vmPFC and the FP. Site 2 receives the strongest inputs from the FP, while site 3 receives the strongest inputs from vmPFC, vlPFC and dlPFC. Site 4 was at the conjunction of areas 32 and 24. It receives the strongest inputs from the OFC, the dlPFC, the dmPFC and the vlPFC. Sites 5 and 6 were in area 24. Site 5 receives the strongest inputs from the OFC and the vlPFC. Site 6 was the closest to

387 the midcingulate cortex. It receives the strongest inputs from the dlPFC, the FEF and the premotor
388 cortex. Site 4 stands out as having the highest number of input areas with the most diverse
389 functional associations. Together with the projection strength patterns across sites, these results
390 suggest that site 4 marks a hub region in the rACC. The dMRI tractography in the NHP
391 demonstrated that streamlines from FC converged in a location comparable to site 4. Using the
392 same tractography methods in human, we found that streamlines from FC also converge in a
393 similar position in the human rACC. Thus, using a cross-species, multimodal approach we
394 demonstrate the existence of a hub in the rACC in NHPs and, in a similar position, a likely hub
395 human rACC.
396
397 *Species homologies*. Comparative studies have utilized spatial location, cytoarchitectonics,
398 connectivity pattern and functional activation to relate homologous areas between human and NHP.
399 The numerical designations of FC areas in early human and NHP atlases (Brodmann, 1909; Walker,
400 1940) have been found most consistent in the dlPFC, while major disagreement exists in ventral
401 and orbital areas (Barbas & Pandya, 1989; Petrides, Tomaiuolo, Yeterian, & Pandya, 2012). Such
402 inconsistency has been further studied and alleviated based on fine-grained cytoarchitectonics and
403 connection patterns (Carmichael & Price, 1995; Mars et al., 2018; Ongur, Ferry, & Price, 2003;
404 Petrides & Pandya, 1994; Petrides et al., 2012). The atlases we used in this study, one by Paxinos
405 et al. (2000) for NHP and the other by Petrides et al. (2012) for human, represent the most up-to-
406 date knowledge of cross-species homology. These atlases were chosen to ensure best possible and
407 accurate comparisons cross species. There are three major divisions of the ACC in NHPs
408 (Morecraft & Tanji, 2009): the sACC (area 25), the pregenual ACC (pACC, area 32 and rostral
409 part of area 24) and the midcingulate (caudal part of area 24). The pACC together with the rostral

410 part of the midcingulate is also referred to as the dACC. In human neuroimaging studies, the
411 definition is less precise. Different from the NHP terminology, the human dACC does not include
412 parts of the pACC but only the rostral part of the midcingulate. The pACC is often referred to as
413 the rACC. To avoid confusion, in this study we use rACC to refer to pACC in both NHPs and
414 humans.
415
416 An important issue is whether the hub is in a homologous region within the rACC. We base our
417 assessment on the surface features and cytoarchitecture of the ACC. The cytoarchitectonic regions
418 of the human cingulate cortex have been found broadly consistent with the NHP region (B. A.
419 Vogt, 2009a; Vogt, Vogt, & Laureys, 2006; Vogt, Nimchinsky, Vogt, & Hof, 1995). The two areas
420 in this study, 32 and 24, occupy the genu of the cingulate cortex in both species. The hub region
421 found by tract tracing was at the conjunction of NHP areas 32 and 24. In human, this conjunction
422 region is located at the rostral-most edge of the cingulate sulcus (Vogt et al., 1995). Thus, using
423 this surface feature as guidance, we compared the human dMRI result (Fig. 8) with a human brain
424 atlas (Mai et al., 2008) to verify that the highest convergent connectivity was near the conjunction
425 of areas 32 and 24.
426
427 *Translation of results between species via dMRI*. Instead of a direct comparison between NHP
428 tracing results and human diffusion tractography, we adopted diffusion tractography in NHP as an
429 intermediate step. Comparing tracing and dMRI results in the same species ensures that dMRI
430 captures the same pathways found by tract tracing. The direct way to replicate the tracing results
431 was to seed at the location of each injection site and trace streamlines to the FC. However, using
432 this method, we found disproportionally fewer streamlines exiting to cortical areas as compared to

433 those that remained within the cingulum bundle (Fig. S2). This problem is due to the dominant
434 fiber orientation in the cingulum bundle. Fibers are highly aligned in the cingulum bundle along
435 the anterior-posterior axis. Consequently, the diffusion signals are strongly anisotropic towards the
436 anterior-posterior direction, while being disproportionally weak in the other directions. Thus,
437 streamlines from the ACC seeds have very low probability of leaving the cingulum bundle. The
438 low number of streamlines reaching different FC areas result in low statistical power for measuring
439 the connectivity pattern. To address this problem, we used seeds in the FC areas instead of the
440 ACC. This way, more streamlines can be traced between an FC area and the ACC, providing
441 sufficient statistical power for estimating the connectivity strength between each area and each
442 ACC voxel (Fig. S2C).
443
444 *Input patterns vs. cytoarchitectonic patterns.* The ACC areal divisions alone cannot fully account
445 for the projection patterns we observed at each site. If the projections were constrained by the
446 cytoarchitectonics of each rACC site, there would be little overlap between the input patterns to
447 sites in area 32 and to those in area 24. Importantly, inputs to site 4 (the hub), positioned at the
448 junction of areas 32 and 24, would equally reflect similarity to the inputs to the neighboring sites
449 3 & 5. However, this was not the case. First, most areas that project to area 32 also project to area
450 24, though with varying strength (Fig. 3). For example, comparing the sets of areas before the 100%
451 cutoff line for sites 1 and 6 in Fig. 3, we found that areas 25, OPro, 13, 47O, OPAl, 9M, 9L, 9/32,
452 8A, 8B, 11 and 47L all project to both sites. Indeed, any pair of sites share common input areas.
453 Second, the input pattern of site 4 was not a simple sum of the input patterns of its neighboring
454 sites 3 & 5. Indeed, site 4 receives strong inputs from areas 8B, 9M, 9/32, 14O and 14M, which
455 do not project strongly to site 3 or 5 (Fig. 5). The inputs to site 4 are uniquely diverse and involves

456 a high number of areas from many FC regions (Figs. 3, 4, & 5). Thus, rather than being predicted
457 by cytoarchitectonics, inputs to the rACC are better understood via three spatial patterns across all
458 sites (Fig. 6).
459
460 *The characterization of a network hub by anatomical projection patterns.* The concept of hub
461 originates from graph theory in brain network analysis (Sporns, 2011). Theoretically, a hub is the
462 node of the highest degree in a network, i.e. with outstandingly numerous connections with the
463 other nodes. In modularized networks as those in the brain, the hub facilitates communication
464 between functional modules. Neuroimaging studies have identified the rACC as a hub of the
465 brain's global network (Buckner et al., 2009; Hagmann et al., 2008). However, the rACC is a large
466 region under the scope of anatomical analysis. Anatomical inputs vary across subregions within
467 the rACC. The hub-like connectivity observed in neuroimaging studies may simply reflect the sum
468 of connections over all of rACC's subregions. The question is then whether a hub exists as a
469 confined subregion within the rACC.
470
471 In this study, site 4 showed two defining features of a hub: high degree of inputs and a position in
472 the network that facilitates cross-module integration. High degree is reflected by the high number
473 of areas with strong projections to this site (Figs. 3-5). To demonstrate cross-module integration,
474 we define functional modules in an empirical manner. The standard graph theory definition
475 requires all-to-all connectivity measured between FC areas (Sporns, 2011). This is impractical with
476 tract tracing experiments. Therefore, instead, we used functional regions of the FC to approximate
477 functional modules. Site 4 marks the most integrative zone in the rACC where inputs from the
478 functional regions converge. First, site 4 is in the central location of two projection gradients. One

479 is formed by inputs from the vmPFC and the FP (Fig. 6A). These are regions associated with
480 emotion and decision making (Joyce & Barbas, 2018; Piray, Toni, & Cools, 2016; Tsujimoto,
481 Genovesio, & Wise, 2010). They project strongly to sites 1-3, less so to sites 4 and 5, and the least
482 to site 6 (Fig. 6A). Inputs from the FEF and the premotor cortex are part of the second gradient.
483 These are motor control regions that project strongly to site 6, less so to sites 4 and 5, and the least
484 to sites 1-3 (Fig. 6B). At each end of the two gradients, the inputs are predominantly associated
485 with emotion- or motor-related functions. Site 4 is in the intermediate transitioning zone of both
486 gradients. Inputs are more balanced between gradients at this site. Second and importantly, a third
487 gradient peaks at site 4. Input strength from regions associated with higher cognition gradually
488 increases from site 1-4 and decrease from site 4-6 (Fig. 6C). The peaking inputs at site 4 allows
489 higher cognition to maximally interface with emotion and motor control. Therefore, site 4 enables
490 communication between all three functional modalities. Together with the high degree of inputs,
491 the integrative nature of site 4 makes it a hub in the prefrontal network.
492
493 *Implications of FC afferent input patterns on ACC functions.* There has been a dichotomy in the
494 classical interpretation of ACC functions, such that emotional and cognitive influences affect the
495 ventral and dorsal ACC separately (Bush, Luu, & Posner, 2000). Classically, the ventral ACC is
496 attributed with "limbic" functions, e.g. visceral responses, emotion, and memory (Buckner,
497 Andrews-Hanna, & Schacter, 2008; Etkin et al., 2015; Mayberg et al., 1999; Papez, 1995; Vogt,
498 Finch, & Olson, 1992). The dorsal ACC is linked with executive control, typically for choosing
499 from conflicting actions and monitoring behavioral outcomes (Botvinick, 2007; Holroyd & Coles,
500 2002; MacDonald, Cohen, Stenger, & Carter, 2000; Pardo, Pardo, Janer, & Raichle, 1990).
501 However, this coarse dichotomy cannot entirely account for the complex activation patterns of the

ACC across an increasing body of experiments. Recent theories have acknowledged the influence of reward and economic evaluation on the executive component of the dorsal ACC function (Botvinick & Braver, 2015; Kolling et al., 2016; Shenhav et al., 2016), even though reward processing is classically thought of as a ventral ACC/vmPFC function. Meanwhile, the effect of cognitive regulation over emotion in the rostral/ventral ACC has also been addressed in the literature on fear extinction (Etkin et al., 2015; Klumpp et al., 2017).

The rACC hub provides an alternative view to the ventral/dorsal dichotomy. Instead of associating each subregion with one function to support serial computation, the ACC may be better understood through the functional integration by its subregions. In neuroimaging studies, the rACC as a large region showed high degree of structural and functional connectivity with the rest of the brain (Buckner et al., 2009; Hagmann et al., 2008). In this study our results further demonstrated that the integration can be carried out in a precise subregion. Site 4 is not simply a conjunction between the ventral and dorsal ACC, but a hub that routes information across functional modules. The inputs to the hub contain strong projections from the vlPFC, the dlPFC and the dmPFC. These regions are critical for higher cognition, such as social behavior (Stalnaker, Cooch, & Schoenbaum, 2015), decision making (Kable & Levy, 2015; Sakagami & Pan, 2007; Wallis, 2007), learning (Atlas, Doll, Li, Daw, & Phelps, 2016; Schuck, Cai, Wilson, & Niv, 2016), attention (Corbetta & Shulman, 2002; Uddin, 2015) and working memory (D'Esposito & Postle, 2015; Miller & Cohen). Thus, the hub can route the outputs of higher cognitive functions to emotion and executive processing within the ventral and dorsal ACC. The hub may be uniquely positioned for evaluating and arbitrating between these processes (van den Heuvel & Sporns, 2013). The detailed

524 mechanisms may be further investigated through connections of the hub and the other subregions
525 of the ACC.
526
527 *Implications on the pathophysiology of psychiatric disorders.* From a network perspective, most
528 psychiatric disorders are seen as a consequence of network imbalance rather than localized deficits
529 (Menon). In light of this view, damage to a hub region can cause disconnection between a wide
530 range of functional modalities, and correspondingly, a spectrum of affective and cognitive
531 disorders. The disconnection hypothesis is in line with the broadly observed rACC abnormality in
532 various diseases, including major depression disorder (MDD) (Mayberg et al., 1997; Pizzagalli,
533 2011), obsessive-compulsive disorder (OCD) (Beucke et al., 2014; Tadayonnejad et al., 2017),
534 attention deficit hyperactivity disorder (Tomasi & Volkow), and posttraumatic stress disorder
535 (Bryant et al., 2008; Kennis, Rademaker, van Rooij, Kahn, & Geuze, 2015; Patel et al., 2012).
536 Based on the FC areas sending convergent inputs to the hub, we propose that dysconnectivity with
537 the hub may be key to understanding the imbalance between goal directed control, emotion and
538 higher cognition in these disorders. MDD and OCD both show treatment response in the rACC
539 activity (Chakrabarty, Ogrodniczuk, & Hadjipavlou, 2016; Fullana et al., 2014; Mayberg et al.,
540 1997; O'Neill & Schultz, 2013; Pizzagalli, 2011). The distinction in their pathophysiology lies in
541 the type of networks involved: MDD engages the networks for self-reference and cognitive control
542 (Pizzagalli, 2011), while OCD engages those for reward-driven and goal-directed behaviors (Milad
543 & Rauch, 2012). The hub connects a majority of FC areas involved in the above networks, which
544 makes it a site prone to damage in both disorders. Moreover, the precise pattern of its anatomical
545 connections provides important information for targeting disorder-specific disconnections and
546 affected areas.

Acknowledgements

The anatomic tracing studies and dMRI analyses were supported by NIH/NIMH grants MH106435, MH045573 and U01-MH109589, and the UK Medical Research Council grant MR/L009013/1. Collection of dMRI animal data was supported in part by the Center for Functional Neuroimaging Technologies (P41-EB015896), Shared Instrumentation Grants S10RR016811, S10RR023401, S10RR019307, and the Human Connectome Project (U01-MH093765). We thank Anna Borkowska-Belanger for expert technical support. The authors declare no conflicts of interest.

References

Andersson, J. L. R., & Sotiropoulos, S. N. (2016). An integrated approach to correction for off-resonance effects and subject movement in diffusion MR imaging. *Neuroimage, 125*, 1063-1078. doi:10.1016/j.neuroimage.2015.10.019

Atlas, L. Y., Doll, B. B., Li, J., Daw, N. D., & Phelps, E. A. (2016). Instructed knowledge shapes feedback-driven aversive learning in striatum and orbitofrontal cortex, but not the amygdala. *Elife, 5*. doi:10.7554/eLife.15192

Barbas, H., & Pandya, D.N. (1989). Architecture and intrinsic connections of the prefrontal cortex in the rhesus monkey. *J. Comp. Neurol., 286*, 353-375.

Behrens, T. E., Berg, H. J., Jbabdi, S., Rushworth, M. F., & Woolrich, M. W. (2007). Probabilistic diffusion tractography with multiple fibre orientations: What can we gain? *Neuroimage, 34*(1), 144-155. doi:10.1016/j.neuroimage.2006.09.018

Beucke, J. C., Sepulcre, J., Eldaief, M. C., Sebold, M., Kathmann, N., & Kaufmann, C. (2014). Default mode network subsystem alterations in obsessive-compulsive disorder. *Br J Psychiatry, 205*(5), 376-382. doi:10.1192/bjp.bp.113.137380

570 Botvinick, M., & Braver, T. (2015). Motivation and cognitive control: from behavior to neural
571 mechanism. *Annu Rev Psychol, 66*, 83-113. doi:10.1146/annurev-psych-010814-015044
572 Botvinick, M. M. (2007). Conflict monitoring and decision making: reconciling two perspectives
573 on anterior cingulate function. *Cogn Affect Behav Neurosci, 7*(4), 356-366.
574 Brodmann, K. (1909). *Vergleichende Lokalisationslehre der Grosshirnrinde*. Leipzig: J.A. Barth.
575 Bryant, R. A., Felmingham, K., Whitford, T. J., Kemp, A., Hughes, G., Peduto, A., & Williams,
576 L. M. (2008). Rostral anterior cingulate volume predicts treatment response to cognitive-
577 behavioural therapy for posttraumatic stress disorder. *J Psychiatry Neurosci, 33*(2), 142-
578 146.
579 Buckner, R. L., Andrews-Hanna, J. R., & Schacter, D. L. (2008). The brain's default network:
580 anatomy, function, and relevance to disease. *Ann N Y Acad Sci, 1124*, 1-38. doi:
581 10.1196/annals.1440.011
582 Buckner, R. L., Sepulcre, J., Talukdar, T., Krienen, F. M., Liu, H., Hedden, T., . . . Johnson, K. A.
583 (2009). Cortical hubs revealed by intrinsic functional connectivity: mapping, assessment
584 of stability, and relation to Alzheimer's disease. *J Neurosci, 29*(6), 1860-1873.
585 doi:10.1523/JNEUROSCI.5062-08.2009
586 Bush, G., Luu, P., & Posner, M. I. (2000). Cognitive and emotional influences in anterior cingulate
587 cortex. *Trends Cogn Sci, 4*(6), 215-222.
588 Calabrese, E., Badea, A., Coe, C. L., Lubach, G. R., Shi, Y., Styner, M. A., & Johnson, G. A.
589 (2015). A diffusion tensor MRI atlas of the postmortem rhesus macaque brain. *Neuroimage,*
590 *117*, 408-416. doi:10.1016/j.neuroimage.2015.05.072
591 Camille, N., Griffiths, C. A., Vo, K., Fellows, L. K., & Kable, J. W. (2011). Ventromedial frontal
592 lobe damage disrupts value maximization in humans. *J Neurosci, 31*(20), 7527-7532. doi:

10.1523/JNEUROSCI.6527-10.2011

Carmichael, S. T., & Price, J. L. (1995). Limbic connections of the orbital and medial prefrontal cortex in macaque monkeys. *Journal of Comparative Neurology, 363*(4), 615-641. doi:10.1002/cne.903630408

Caruana, F., Gerbella, M., Avanzini, P., Gozzo, F., Pelliccia, V., Mai, R., . . . Rizzolatti, G. (2018). Motor and emotional behaviours elicited by electrical stimulation of the human cingulate cortex. *Brain*. doi:10.1093/brain/awy219

Chakrabarty, T., Ogrodniczuk, J., & Hadjipavlou, G. (2016). Predictive Neuroimaging Markers of Psychotherapy Response: A Systematic Review. *Harv Rev Psychiatry, 24*(6), 396-405. doi:10.1097/HRP.0000000000000132

Choi, E. Y., Tanimura, Y., Vage, P. R., Yates, E. H., & Haber, S. N. (2016). Convergence of prefrontal and parietal anatomical projections in a connectional hub in the striatum. *Neuroimage*. doi:10.1016/j.neuroimage.2016.09.037

Cisek, P. (2012). Making decisions through a distributed consensus. *Curr Opin Neurobiol, 22*(6), 927-936. doi:10.1016/j.conb.2012.05.007

Clark, D.L., Boutros, N.N., & Mendez, M.F. (2010). *The Brain and Behavior: An Introduction to Behavioral Neuroanatomy*: Cambridge University Press.

Conrad, Keith (2004). Probability distributions and maximum entropy. *J Entropy, 6*(452), 10.

Corbetta, M., & Shulman, G. L. (2002). Control of goal-directed and stimulus-driven attention in the brain. *Nat Rev Neurosci, 3*(3), 201-215. doi:10.1038/nrn755

D'Esposito, M., & Postle, B. R. (2015). The cognitive neuroscience of working memory. *Annu Rev Psychol, 66*, 115-142. doi:10.1146/annurev-psych-010814-015031

615 Etkin, A., Buchel, C., & Gross, J. J. (2015). The neural bases of emotion regulation. *Nat Rev*
616 *Neurosci, 16*(11), 693-700. doi:10.1038/nrn4044
617 Fan, Q., Witzel, T., Nummenmaa, A., Van Dijk, K. R., Van Horn, J. D., Drews, M. K., . . . Rosen,
618 B. R. (2016). MGH-USC Human Connectome Project datasets with ultra-high b-value
619 diffusion MRI. *Neuroimage, 124*(Pt B), 1108-1114.
620 doi:10.1016/j.neuroimage.2015.08.075
621 Fullana, M. A., Cardoner, N., Alonso, P., Subira, M., Lopez-Sola, C., Pujol, J., . . . Soriano-Mas,
622 C. (2014). Brain regions related to fear extinction in obsessive-compulsive disorder and its
623 relation to exposure therapy outcome: a morphometric study. *Psychol Med, 44*(4), 845-856.
624 doi:10.1017/S0033291713001128
625 Haber, S. N., Kim, K. S., Mailly, P., & Calzavara, R. (2006). Reward-related cortical inputs define
626 a large striatal region in primates that interface with associative cortical connections,
627 providing a substrate for incentive-based learning. *J Neurosci, 26*(32), 8368-8376.
628 doi:10.1523/JNEUROSCI.0271-06.2006
629 Hagmann, P., Cammoun, L., Gigandet, X., Meuli, R., Honey, C. J., Wedeen, V. J., & Sporns, O.
630 (2008). Mapping the structural core of human cerebral cortex. *PLoS Biol, 6*(7), e159.
631 doi:10.1371/journal.pbio.0060159
632 Holroyd, C. B., & Coles, M. G. (2002). The neural basis of human error processing: reinforcement
633 learning, dopamine, and the error-related negativity. *Psychol Rev, 109*(4), 679-709.
634 Hunt, L. T., Woolrich, M. W., Rushworth, M. F., & Behrens, T. E. (2013). Trial-type dependent
635 frames of reference for value comparison. *PLoS Comput Biol, 9*(9), e1003225.
636 doi:10.1371/journal.pcbi.1003225

637 Jenkinson, M., Beckmann, C. F., Behrens, T. E., Woolrich, M. W., & Smith, S. M. (2012). Fsl.
638 *Neuroimage, 62*(2), 782-790. doi:10.1016/j.neuroimage.2011.09.015
639 Jiang, J., Beck, J., Heller, K., & Egner, T. (2015). An insula-frontostriatal network mediates
640 flexible cognitive control by adaptively predicting changing control demands. *Nat*
641 *Commun, 6*, 8165. doi:10.1038/ncomms9165
642 Jocham, G., Hunt, L. T., Near, J., & Behrens, T. E. (2012). A mechanism for value-guided choice
643 based on the excitation-inhibition balance in prefrontal cortex. *Nat Neurosci, 15*(7), 960-
644 961. doi:10.1038/nn.3140
645 Joyce, M. K. P., & Barbas, H. (2018). Cortical Connections Position Primate Area 25 as a Keystone
646 for Interoception, Emotion, and Memory. *J Neurosci, 38*(7), 1677-1698.
647 doi:10.1523/JNEUROSCI.2363-17.2017
648 Kable, J. W., & Glimcher, P. W. (2009). The neurobiology of decision: consensus and controversy.
649 *Neuron, 63*(6), 733-745. doi:10.1016/j.neuron.2009.09.003
650 Kable, J. W., & Levy, I. (2015). Neural markers of individual differences in decision-making. *Curr*
651 *Opin Behav Sci, 5*, 100-107. doi:10.1016/j.cobeha.2015.08.004
652 Kennis, M., Rademaker, A. R., van Rooij, S. J., Kahn, R. S., & Geuze, E. (2015). Resting state
653 functional connectivity of the anterior cingulate cortex in veterans with and without post-
654 traumatic stress disorder. *Hum Brain Mapp, 36*(1), 99-109. doi:10.1002/hbm.22615
655 Klein, S., Staring, M., Murphy, K., Viergever, M. A., & Pluim, J. P. (2010). elastix: a toolbox for
656 intensity-based medical image registration. *IEEE Trans Med Imaging, 29*(1), 196-205.
657 doi:10.1109/TMI.2009.2035616
658 Klumpp, H., Roberts, J., Kennedy, A. E., Shankman, S. A., Langenecker, S. A., Gross, J. J., &
659 Phan, K. L. (2017). Emotion regulation related neural predictors of cognitive behavioral

therapy response in social anxiety disorder. *Prog Neuropsychopharmacol Biol Psychiatry, 75*, 106-112. doi:10.1016/j.pnpbp.2017.01.010

Kolling, N., Behrens, T. E., Mars, R. B., & Rushworth, M. F. (2012). Neural mechanisms of foraging. *Science, 336*(6077), 95-98. doi:10.1126/science.1216930

Kolling, N., Scholl, J., Chekroud, A., Trier, H. A., & Rushworth, M. F. S. (2018). Prospection, Perseverance, and Insight in Sequential Behavior. *Neuron, 99*(5), 1069-1082 e1067. doi:10.1016/j.neuron.2018.08.018

Kolling, N., Wittmann, M. K., Behrens, T. E., Boorman, E. D., Mars, R. B., & Rushworth, M. F. (2016). Value, search, persistence and model updating in anterior cingulate cortex. *Nat Neurosci, 19*(10), 1280-1285. doi:10.1038/nn.4382

Lee, S. W., Shimojo, S., & O'Doherty, J. P. (2014). Neural computations underlying arbitration between model-based and model-free learning. *Neuron, 81*(3), 687-699. doi:10.1016/j.neuron.2013.11.028

MacDonald, A. W. 3rd, Cohen, J. D., Stenger, V. A., & Carter, C. S. (2000). Dissociating the role of the dorsolateral prefrontal and anterior cingulate cortex in cognitive control. *Science, 288*, 1835-1839.

Mai, J., Paxinos, G, & Voss, T. (2008). *Atlas of the Human Brain*: Elsevier.

Mars, R. B., Sotiropoulos, S. N., Passingham, R. E., Sallet, J., Verhagen, L., Khrapitchev, A. A., . . . Jbabdi, S. (2018). Whole brain comparative anatomy using connectivity blueprints. *Elife, 7*. doi:10.7554/eLife.35237

Mayberg, H. S., Brannan, S. K., Mahurin, R. K., Jerabek, P. A., Brickman, J. S., Tekell, J. L., . . . Fox, P. T. (1997). Cingulate function in depression: a potential predictor of treatment response. *Neuroreport, 8*(4), 1057-1061.

683 Mayberg, H. S., Liotti, M., Brannan, S. K., McGinnis, S., Mahurin, R. K., Jerabek, P. A., . . . Fox,
684 P. T. (1999). Reciprocal limbic-cortical function and negative mood: converging PET
685 findings in depression and normal sadness. *American Journal of Psychiatry, 156*(5), 675-
686 682.
687 Menon, V. (2011). Large-scale brain networks and psychopathology: a unifying triple network
688 model. *Trends Cogn Sci, 15*(10), 483-506. doi:10.1016/j.tics.2011.08.003
689 Milad, M. R., & Rauch, S. L. (2012). Obsessive-compulsive disorder: beyond segregated cortico-
690 striatal pathways. *Trends Cogn Sci, 16*(1), 43-51. doi:10.1016/j.tics.2011.11.003
691 Miller, E.K., & Cohen, J.D. (2001). An integrative theory of prefrontal cortex function. *Annu. Rev.*
692 *Neurosci., 24*, 167-202.
693 Morecraft, R. J., Stilwell-Morecraft, K. S., Cipolloni, P. B., Ge, J., McNeal, D. W., & Pandya, D.
694 N. (2012). Cytoarchitecture and cortical connections of the anterior cingulate and adjacent
695 somatomotor fields in the rhesus monkey. *Brain Res Bull, 87*(4-5), 457-497.
696 doi:10.1016/j.brainresbull.2011.12.005
697 Morecraft, Robert J, & Tanji, Jun. (2009). Cingulofrotnal interactions and the cingulate motor
698 areas. In Brent A. Vogt (Ed.), *Cingulate neurobiology and disease* (pp. 113-144). Oxford ;
699 New York: Oxford University Press.
700 O'Neill, M., & Schultz, W. (2013). Risk prediction error coding in orbitofrontal neurons. *J*
701 *Neurosci, 33*(40), 15810-15814. doi:10.1523/JNEUROSCI.4236-12.2013
702 Ongur, D., Ferry, A. T., & Price, J. L. (2003). Architectonic subdivision of the human orbital and
703 medial prefrontal cortex. *J Comp Neurol, 460*(3), 425-449.
704 Ongur, D., & Price, J. L. (2000). The organization of networks within the orbital and medial
705 prefrontal cortex of rats, monkeys and humans. *Cerebral Cortex, 10*(3), 206-219.

706 Pandya, D.N., & Seltzer, B. (1982). Association areas of the cerebral cortex. *Trends Neurosci., 5*,
707 386-390.
708 Papez, J.W. (1995). A proposed mechanism of emotion. 1937. *J Neuropsychiatry Clin Neurosci,*
709 *7*, 103-112.
710 Pardo, J. V., Pardo, P. J., Janer, K. W., & Raichle, M. E. (1990). The anterior cingulate cortex
711 mediates processing selection in the Stroop attentional conflict paradigm. *Proceedings of*
712 *the National Academy of Sciences of the United States of America, 87*(1), 256-259.
713 Patel, S. R., Sheth, S. A., Mian, M. K., Gale, J. T., Greenberg, B. D., Dougherty, D. D., & Eskandar,
714 E. N. (2012). Single-neuron responses in the human nucleus accumbens during a financial
715 decision-making task. *J Neurosci, 32*(21), 7311-7315. doi:10.1523/JNEUROSCI.0027-
716 12.2012
717 Paxinos, G ., Huang, X. F., & Toga, A. W. (2000). *The rhesus monkey in stereotaxic coordinates*.
718 San Diego: Academic Press.
719 Petrides, M., & Pandya, D. N. (1994). Comparative architectonic analysis of the human and
720 macaque frontal cortex. In F. Boller & J. Grafman (Eds.), *Handbook of Neuropsychology*
721 (pp. 17-58). Amsterdam: Elsevier.
722 Petrides, M., Tomaiuolo, F., Yeterian, E. H., & Pandya, D. N. (2012). The prefrontal cortex:
723 comparative architectonic organization in the human and the macaque monkey brains.
724 *Cortex, 48*(1), 46-57. doi:10.1016/j.cortex.2011.07.002
725 Picard, N., & Strick, P.L. (1996). Motor areas of the medial wall: A review of their location and
726 functional activation. *Cereb. Cortex, 6*, 342-353.

727 Piray, P., Toni, I., & Cools, R. (2016). Human Choice Strategy Varies with Anatomical Projections
728 from Ventromedial Prefrontal Cortex to Medial Striatum. *J Neurosci, 36*(10), 2857-2867.
729 doi:10.1523/JNEUROSCI.2033-15.2016
730 Pizzagalli, D. A. (2011). Frontocingulate dysfunction in depression: toward biomarkers of
731 treatment response. *Neuropsychopharmacology, 36*(1), 183-206.
732 doi:10.1038/npp.2010.166
733 Preuss, T.M., & Goldman-Rakic, P.S. (1991). Myelo-and cytoarchitecture of the granular frontal
734 cortex and surrounding regions in the strepsirhine primate galago and the anthropoid
735 primate macaca. *J. Comp. Neurol., 310*, 429-474.
736 Rangel, A., & Hare, T. (2010). Neural computations associated with goal-directed choice. *Curr*
737 *Opin Neurobiol, 20*(2), 262-270. doi:10.1016/j.conb.2010.03.001
738 Rushworth, M. F., Kolling, N., Sallet, J., & Mars, R. B. (2012). Valuation and decision-making in
739 frontal cortex: one or many serial or parallel systems? *Curr Opin Neurobiol, 22*(6), 946-
740 955. doi:10.1016/j.conb.2012.04.011
741 Safadi, Z., Grisot, G., Jbabdi, S., Behrens, T. E., Heilbronner, S. R., McLaughlin, N. C. R., . . .
742 Haber, S. N. (2018). Functional Segmentation of the Anterior Limb of the Internal Capsule:
743 Linking White Matter Abnormalities to Specific Connections. *J Neurosci, 38*(8), 2106-
744 2117. doi:10.1523/JNEUROSCI.2335-17.2017
745 Sakagami, M., & Pan, X. (2007). Functional role of the ventrolateral prefrontal cortex in decision
746 making. *Curr Opin Neurobiol, 17*(2), 228-233. doi:10.1016/j.conb.2007.02.008
747 Schuck, N. W., Cai, M. B., Wilson, R. C., & Niv, Y. (2016). Human Orbitofrontal Cortex
748 Represents a Cognitive Map of State Space. *Neuron, 91*(6), 1402-1412.
749 doi:10.1016/j.neuron.2016.08.019

750 Shadlen, MN, Kiani, R, Hanks, TD, & Churchland, AK. (2008). Neurobiology of Decision Making:
751 An Intentional Framework. In C. Engel and W. Singer (Ed.), *Better Than Conscious?*
752 *Decision Making, the Human Mind, and Implications For Institutions*: MIT Press:
753 Cambridge.
754 Shenhav, A., Cohen, J. D., & Botvinick, M. M. (2016). Dorsal anterior cingulate cortex and the
755 value of control. *Nat Neurosci, 19*(10), 1286-1291. doi:10.1038/nn.4384
756 Sporns, Olaf. (2011). *Networks of the brain*. Cambridge, Mass.: MIT Press.
757 Stalnaker, T. A., Cooch, N. K., & Schoenbaum, G. (2015). What the orbitofrontal cortex does not
758 do. *Nat Neurosci, 18*(5), 620-627. doi:10.1038/nn.3982
759 Tadayonnejad, R., Deshpande, R., Ajilore, O., Moody, T., Morfini, F., Ly, R., . . . Feusner, J. D.
760 (2017). Pregenual Anterior Cingulate Dysfunction Associated with Depression in OCD:
761 An Integrated Multimodal fMRI/(1)H MRS Study. *Neuropsychopharmacology*.
762 doi:10.1038/npp.2017.249
763 Tomasi, D., & Volkow, N. D. (2012). Abnormal functional connectivity in children with attention-
764 deficit/hyperactivity disorder. *Biol Psychiatry, 71*(5), 443-450.
765 doi:10.1016/j.biopsych.2011.11.003
766 Tsujimoto, S., Genovesio, A., & Wise, S. P. (2010). Evaluating self-generated decisions in frontal
767 pole cortex of monkeys. *Nat Neurosci, 13*(1), 120-126. doi:10.1038/nn.2453
768 Uddin, L. Q. (2015). Salience processing and insular cortical function and dysfunction. *Nat Rev*
769 *Neurosci, 16*(1), 55-61. doi:10.1038/nrn3857
770 van den Heuvel, M. P., & Sporns, O. (2013). Network hubs in the human brain. *Trends Cogn Sci,*
771 *17*(12), 683-696. doi:10.1016/j.tics.2013.09.012

772 Vogt, B. A. (2009a). Architecture, Neurocytology and Comparative Organization of Monkey and
773 Human Cingulate Cortices. In B. A. Vogt (Ed.), *Cingulate Neurobiology and Disease* (pp.
774 66-93). Oxford: Oxford University Press.
775 Vogt, B. A. (2009b). Regions and subregions of the Cingulate Cortex. In B. A. Vogt (Ed.),
776 *Cingulate Neurobiology and Disease* (pp. 3-30). Oxford: Oxford University Press.
777 Vogt, B. A., Vogt, L., & Laureys, S. (2006). Cytology and functionally correlated circuits of
778 human posterior cingulate areas. *Neuroimage, 29*(2), 452-466.
779 doi:10.1016/j.neuroimage.2005.07.048
780 Vogt, B.A. (1993a). *Neurobiology of cingulate cortex and limbic thalamus*. Boston: Birkhäuser.
781 Vogt, B.A. (1993b). Structural organization of cingulate cortex: areas, neurons and
782 somatodendritic receptors. In B.A. Vogt & M. Gabriel (Eds.), *Neurobiology of cingulate*
783 *cortex and limbic thalamus* (pp. 19-70). Boston: Birkhäuser.
784 Vogt, B.A., Finch, D.M., & Olson, C.R. (1992). Functional heterogeneity in cingulate cortex: The
785 anterior executive and posterior evaluative regions. *Cereb. Cortex, 2*, 435-443.
786 Vogt, B.A., Nimchinsky, E.A., Vogt, L.J., & Hof, P.R. (1995). Human cingulate cortex: Surface
787 features, flat maps, and cytoarchitecture. *J. Comp. Neurol., 359*, 490-506.
788 Vogt, Brent A. (2009). *Cingulate neurobiology and disease*. Oxford ; New York: Oxford
789 University Press.
790 Walker, A.E. (1940). A cytoarchitectural study of the prefronal area of the macaque monkey. *J.*
791 *Comp. Neurol., 73*, 59-86.
792 Wallis, J. D. (2007). Orbitofrontal cortex and its contribution to decision-making. *Annu Rev*
793 *Neurosci, 30*, 31-56. doi:10.1146/annurev.neuro.30.051606.094334

794

795 **Figure Legends**

796 Figure 1. Injection sites and cortical area definition. (A) Locations of the 7 out of 16 ACC
797 injections that were selected for stereology analysis. Six cases (red) were analyzed as the main
798 result and the additional one (blue) as control. The numbering of cases followed the longitudinal
799 axis of the cingulate gyrus. Cases not used for stereology due to the limitation in transport,
800 background and location were colored beige. The cortex of the right hemisphere is shown in semi-
801 transparent brown, the corpus callosum in white, and the cingulate sulcus and rostral sulcus in
802 purple and cyan. (B) Photomicrographs to show the histology of each injection site. (C) Section
803 outline of FC areas on an example slide. The borders between areas were hand-drawn following
804 the atlas by Paxino et al. (2008).

805

806 Figure 2. Retrogradely labeled cells (red) in cases 1–6. Each column contains rostral to caudal
807 coronal sections from one case. Sections of the same row have matching locations along the rostro-
808 caudal axis. FC areas are labeled in the first column. Areas not matching the parcellation in the
809 first column were labeled additionally on the corresponding sections.

810

811 Figure 3. Cumulative percent cell count across areas in cases 1–6. Cutoff remarks: green line =
812 50%, red line = 75%, grey line = 100%. Areas after 100% are in a random order. The slope of each
813 curve indicates deviation from a uniform distribution (steeper slope = further deviation).

814

815 Figure 4. Quantitative comparison of cell distributions in cases 1–6. (A) The number of areas that
816 contributed 50% (green) and 75% (red) of inputs in each case. The highest number was found in
817 case 4. (B) The entropy of cell distribution in each case. Higher entropy corresponds to less

818 deviation from the uniform distribution, i.e. more evenly distributed labeled cells across areas. The
819 highest entropy was in case 4.
820
821 Figure 5. Schematic illustration of the FC regions with strong projections in each case. The dashed
822 contour represents the ACC and the circles injections of cases 1–6. The filled circle marks the case
823 being shown. Colored branches represent brain areas that accounted for 75% cell counts in each
824 case (green = adds up to 50%; green + red = adds up to 75%). The most extensive FC regions with
825 strong input was found in case 4.
826
827 Figure 6. Projection strength from different FC regions at each site. Percent scores of inputs from
828 (A) FP & vmPFC, (B) FEF & premotor cortex, (C) dlPFC, dmPFC & vlPFC and (D) OFC are
829 shown in separate panels. In each panel, the percent scores of areas in the corresponding regions
830 were averaged. The mean and standard error across areas are shown for each site. The mean percent
831 score of FP & vmPFC was greater at sites 1-3 than at sites 4-6; that of FEF and premotor cortex
832 was lower at sites 1-3 than at sites 4-6. The mean percent score of dlPFC, dmPFC and vlPFC
833 gradually increases from site 1-4 and decreases from site 4-6. There was no consistent pattern in
834 the OFC percent scores across sites.
835
836 Figure 7. Localization of the hub region in the monkey rACC using dMRI tractography. (A) A
837 coronal section illustrating the Paxinos atlas in the dMRI space provided by Duke University. (B)
838 A coronal section of the atlas brain showing two example seed masks for areas 11 (red) and 46D
839 (green). (C) A sagittal section of an individual monkey brain showing the probabilistic streamline
840 terminals in the rACC, separately for the seeds in area 11 (red) and 46D (green). Voxels with

841 overlapping terminals were in orange. (D) A sagittal section showing the localized hub in 7
842 individual monkeys. Each red dot marks the center of the hub region in one monkey. The center
843 of the hub was defined by the voxel with the highest weighted-sum of probabilistic streamlines
844 from all 29 seeded areas.
845
846 Figure 8. Probabilistic streamlines converging in the rACC in human dMRI. (A) Parcellation of
847 the FC areas on the *fsaverage* template (FreeSurfer 4.5), following Petrides et al. (2012). The
848 FreeSurfer labels are available in the Supplementary File. (B) Sagittal sections showing the
849 localized hub across individuals. Each red dot marks the center of the hub region in one subject.
850 The center of the hub was defined by the voxel with the highest weighted-sum of probabilistic
851 streamlines from all seeded FC areas.
852
853 Figure S1. Percent scores of retrogradely labeled cells were not dominated by the size of the
854 injection site or that of the FC areas. (A) Total number of labeled cells in each case. (B) Cumulative
855 percent cell count across areas, showing only 2 areas contributing to 50% and 5 areas 75% of total
856 inputs. Cutoff remarks: green line = 50%, red line = 75%, grey line = 100%. Areas after 100% are
857 in a random order. (C) Percent scores of labeled cells projecting to each site were not determined
858 by the size of FC areas. The size was measured as the volume of each area divided by the total
859 volume of all areas. Colors mark different sites.
860
861 Figure S2. Difference in the tract strength pattern due to seeding procedures. (A) A seed mask in
862 the rACC. (B) Probabilistic map of the streamlines from the rACC seed to all the other voxels in
863 the brain, showing the dominant high values in the cingulum bundle. (C) Comparison of the

probabilistic streamline distributions with the tract tracing result. The percent score for tracing is based on cell counts, and that for tractography is based on the tract density between the seed and the target masks (values in the fdt_path output by FSL). The tract strength by seeding the FC areas was more correlated (Pearson's coefficient = 0.42, $p < 0.05$) with the tract tracing result than that by seeding the rACC (Pearson's coefficient = 0.17, $p > 0.05$).

Tables

Table 1: List of the 27 frontal areas.

vmPFC	dmFPC	OFC	vlPFC	dlPFC	FEF	Premotor
10L	9M	11	47/47L	9/46V	8A	6L
10M	6M	13	47O	9/46D	8B	6/32
14M	9/32	OPro	44	46	8/32	ProM
14O		OPAl	45A	9L		
25			45B			

Table 2: Summary of the major FC inputs to each site.

Site	# areas contributing 50% inputs	Regions contributing 50% inputs	# areas contributing 75% inputs	Regions contributing additional 25% inputs
1	2	FP, vmPFC	4	FP, OFC
2	2	FP	4	vmPFC, dlPFC
3	3	vmPFC, vlPFC, dlPFC	6	FP, OFC, dlPFC
4	5	OFC, vlPFC, dmPFC, dlPFC	10	vmPFC, OFC, dmPFC, dlPFC, FEF
5	2	OFC, vlPFC	6	FP, vmPFC, OFC, dlPFC
6	4	dlPFC, FEF, Premotor	8	FEF, Premotor

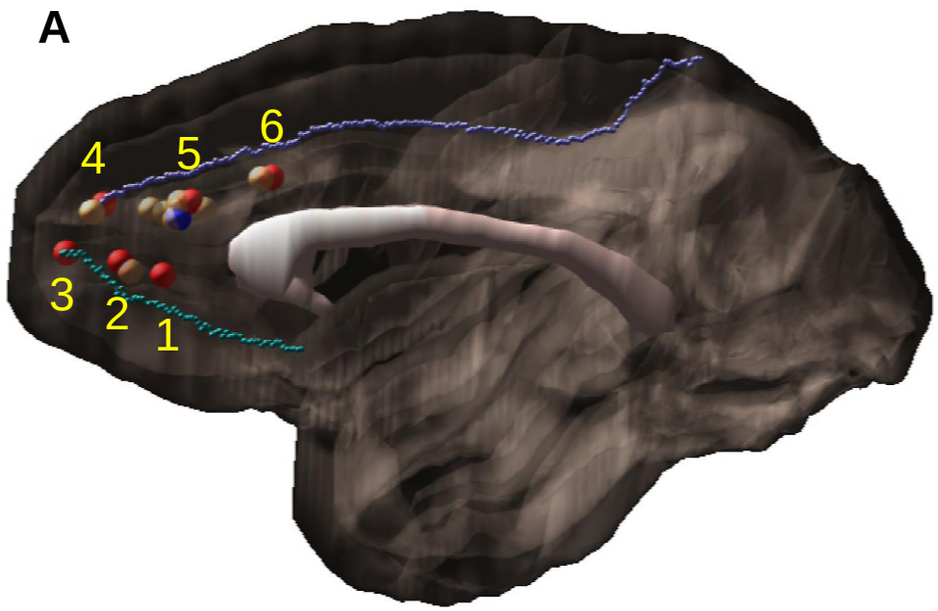
A
4
5
6
3
2
1

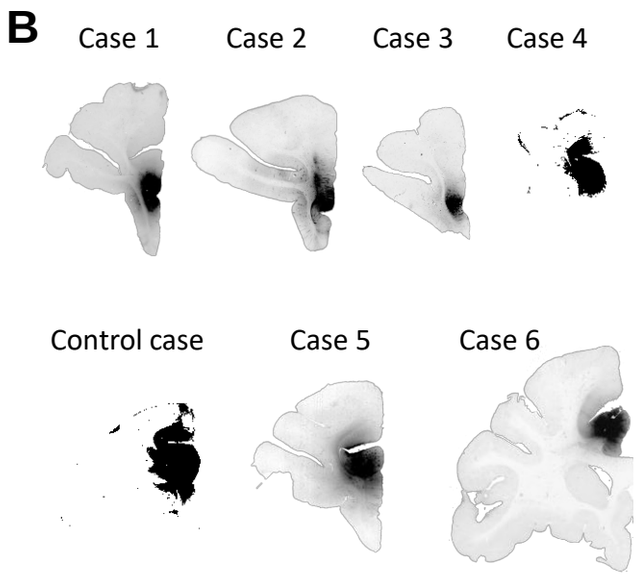
B
Case 1
Case 2
Case 3
Case 4
Control case
Case 5
Case 6

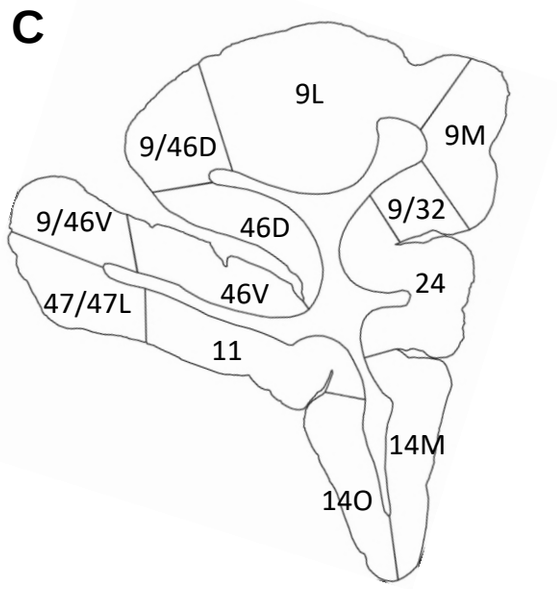
C
9L
9M
9/46D
9/32
9/46V
46D
24
46V
47/47L
11
14M
14O

Figure 2

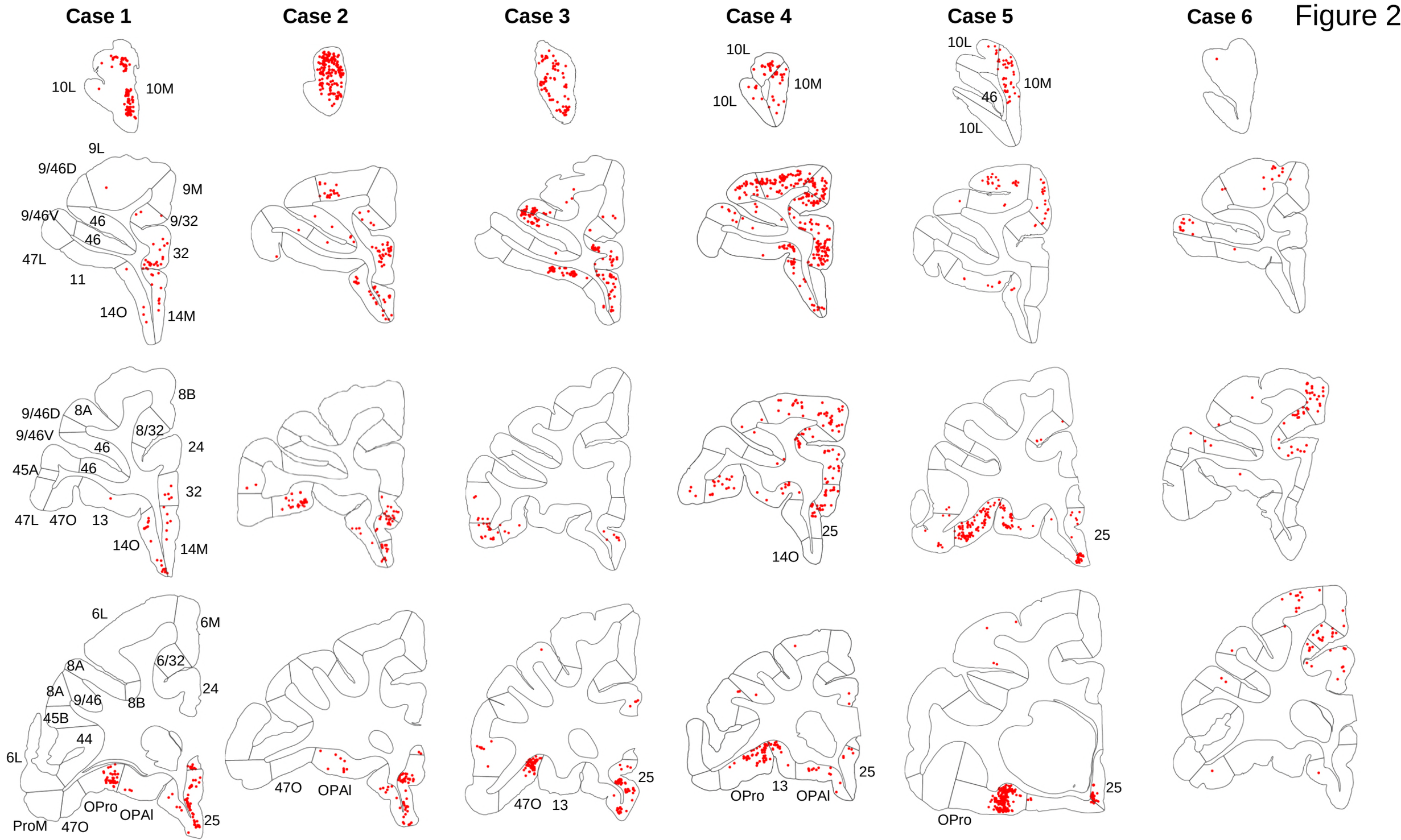
Case 1
Case 2
Case 3
Case 4
Case 5
Case 6
10L
10M
9L
9/46D
9M
9/46V
46
9/32
46
32
47L
11
14O
14M
8B
9/46D
8A
8/32
9/46V
46
24
45A
46
32
47L
47O
13
14O
14M
6L
6M
6/32
8A
24
8A
9/46
8B
45B
44
6L
OPro
OPAl
ProM
47O
25
47O
OPAl
47O
13
25
10L
10M
10L
10L
46
10M
10L
25
14O
25
25
OPro
13
OPAl
25
OPro
25

Figure 3

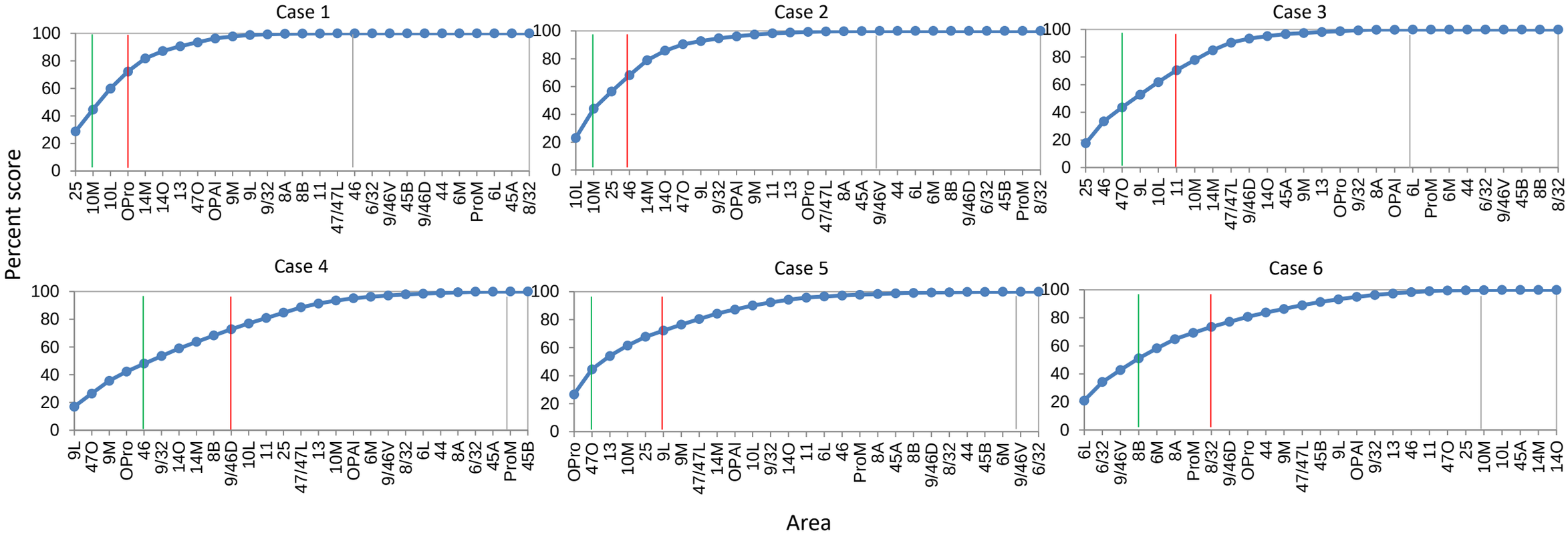

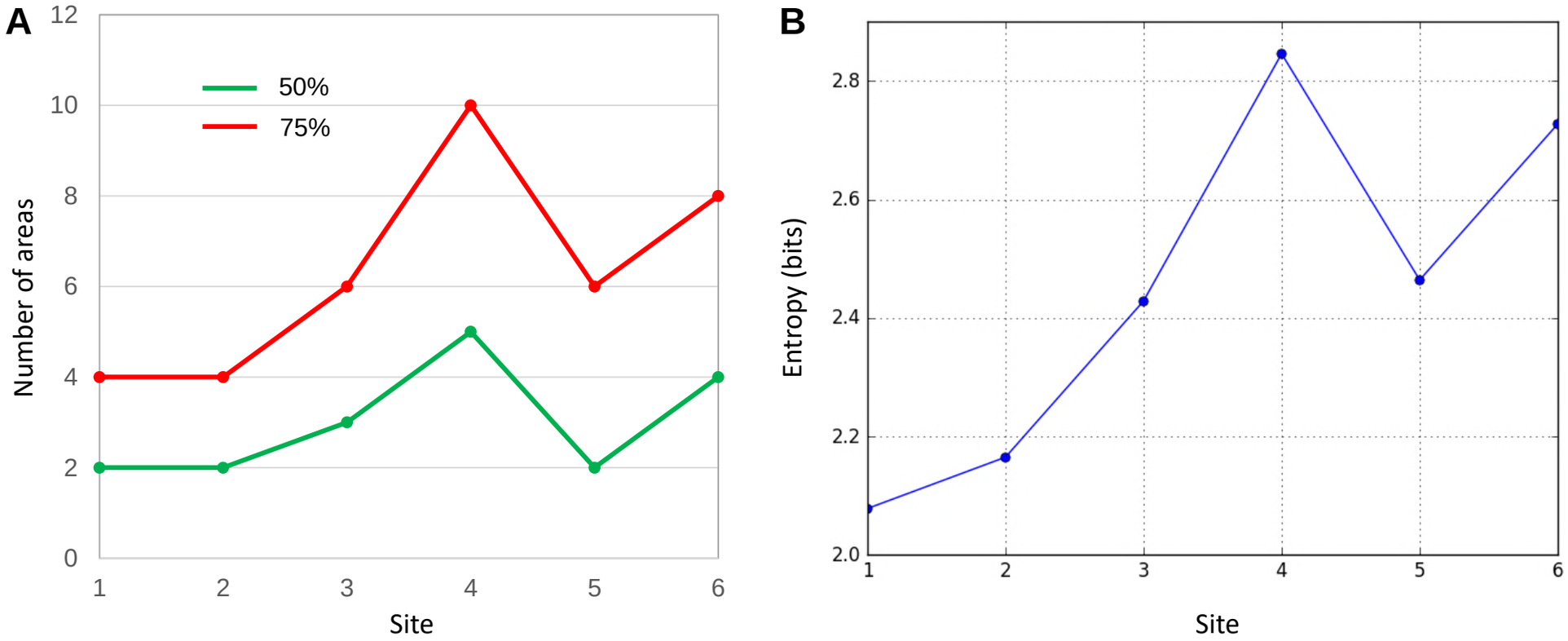
A
12
10
8
6
4
2
0
50%
75%
Number of areas
1
2
3
4
5
6
Site
B
2.8
2.6
2.4
2.2
2.0
Entropy (bits)
1
2
3
4
5
6
Site

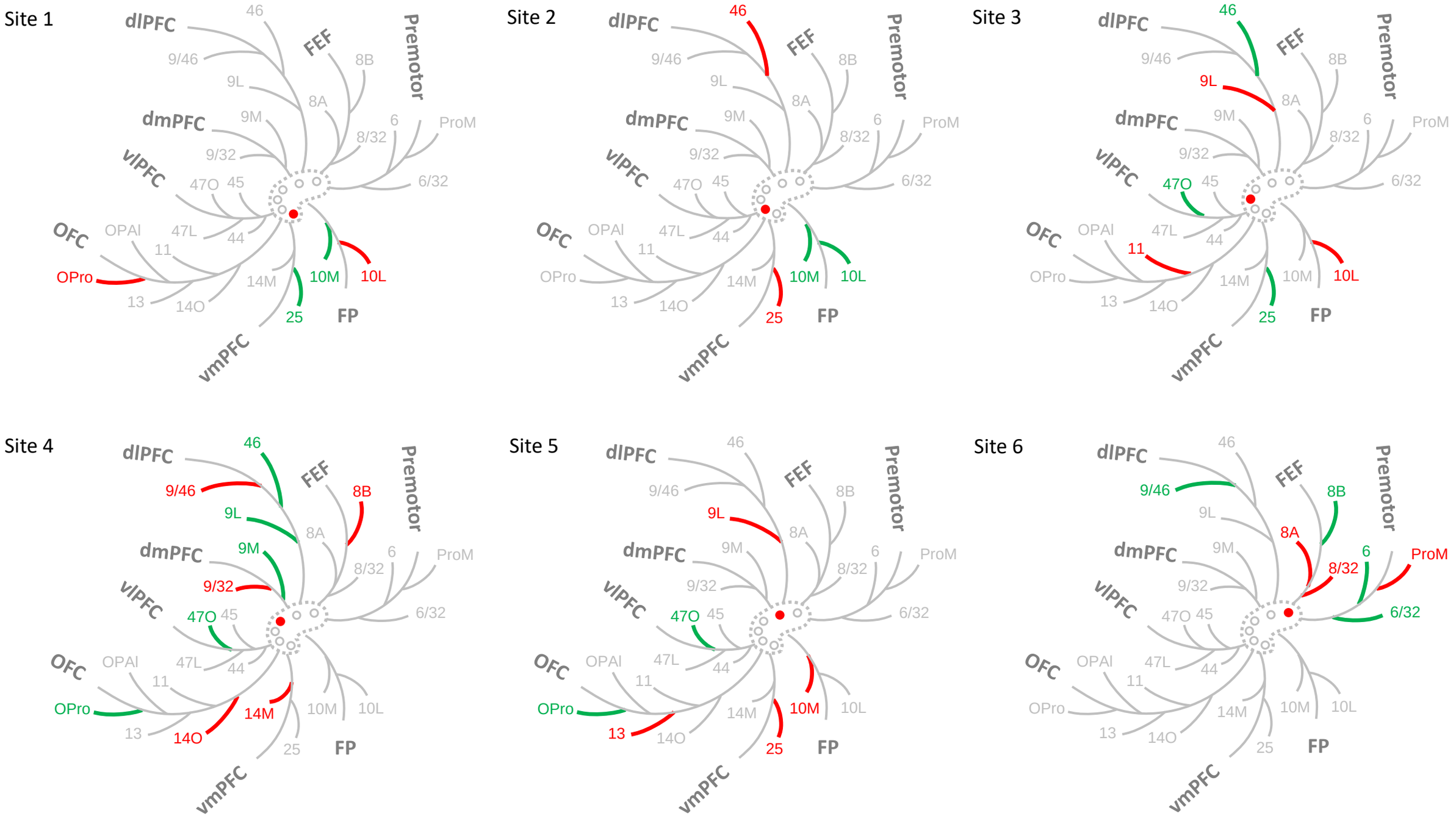
Site 1
dlPFC
46
FEF
Premotor
9/46
8B
9L
8A
dmPFC
9M
6
ProM
8/32
9/32
vlPFC
6/32
47O
45
OFC
OPAI
47L
44
11
OPro
14M
10M
10L
13
14O
25
FP
vmPFC
Site 2
dlPFC
46
FEF
Premotor
9/46
8B
9L
8A
dmPFC
9M
6
ProM
8/32
9/32
vlPFC
6/32
47O
45
OFC
OPAI
47L
44
11
OPro
14M
10M
10L
13
14O
25
FP
vmPFC
Site 3
dlPFC
46
FEF
Premotor
9/46
9L
8B
8A
dmPFC
9M
6
ProM
8/32
9/32
vlPFC
6/32
47O
45
OFC
OPAI
47L
44
11
OPro
14M
10M
10L
13
14O
25
FP
vmPFC
Site 4
dlPFC
46
FEF
Premotor
9/46
8B
9L
8A
dmPFC
9M
6
ProM
8/32
9/32
vlPFC
6/32
47O
45
OFC
OPAI
47L
44
11
OPro
14M
10M
10L
13
14O
25
FP
vmPFC
Site 5
dlPFC
46
FEF
Premotor
9/46
8B
9L
8A
dmPFC
9M
6
ProM
8/32
9/32
vlPFC
6/32
47O
45
OFC
OPAI
47L
44
11
OPro
14M
10M
10L
13
14O
25
FP
vmPFC
Site 6
dlPFC
46
FEF
Premotor
9/46
8B
9L
8A
dmPFC
9M
6
ProM
8/32
9/32
vlPFC
6/32
47O
45
OFC
OPAI
47L
44
11
OPro
14M
10M
10L
13
14O
25
FP
vmPFC

Figure 5

Figure 6

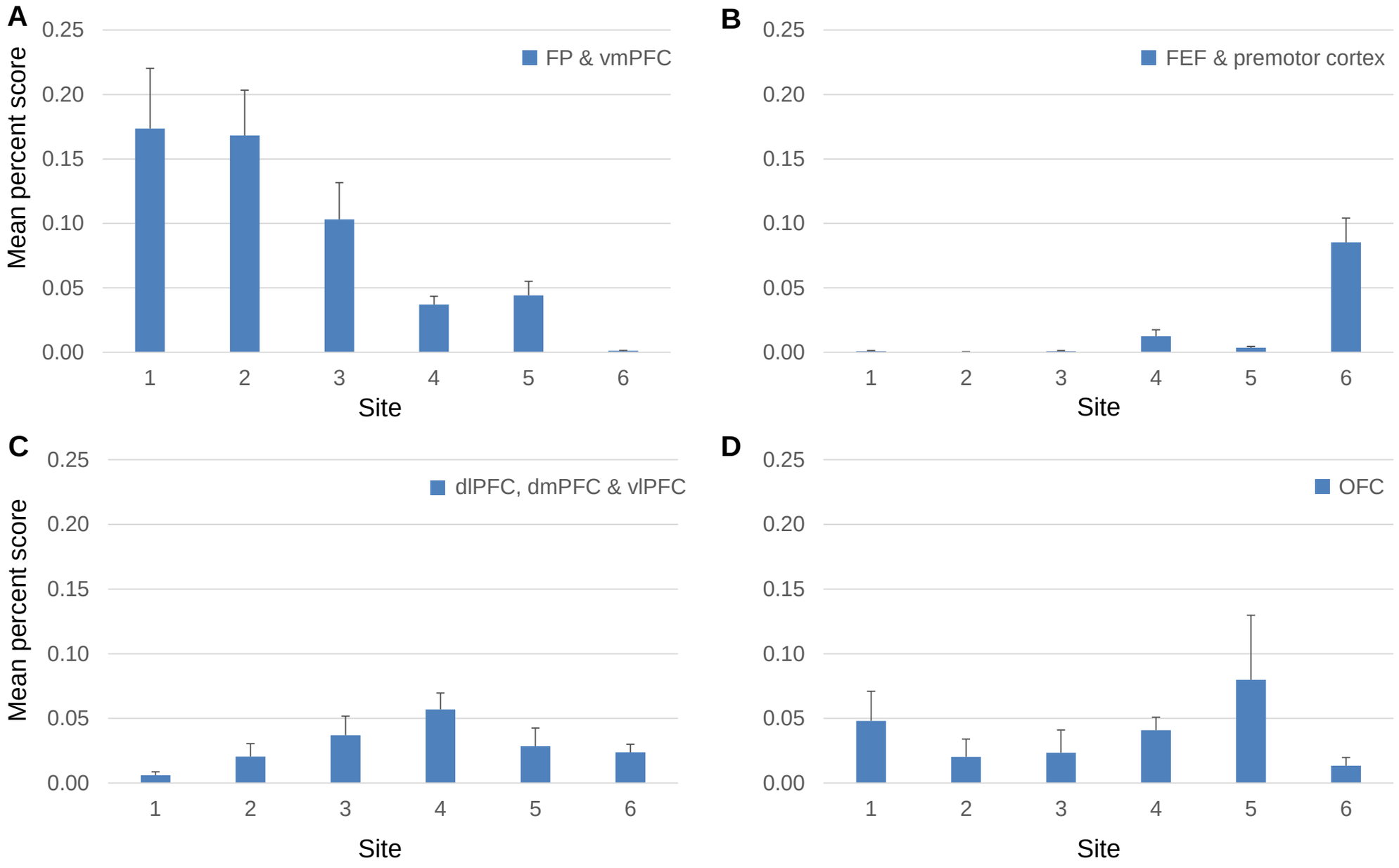
A
Mean percent score
0.25
0.20
0.15
0.10
0.05
0.00
FP & vmPFC
1
2
3
4
5
6
Site
B
FEF & premotor cortex
C
dlPFC, dmPFC & vlPFC
D
OFC

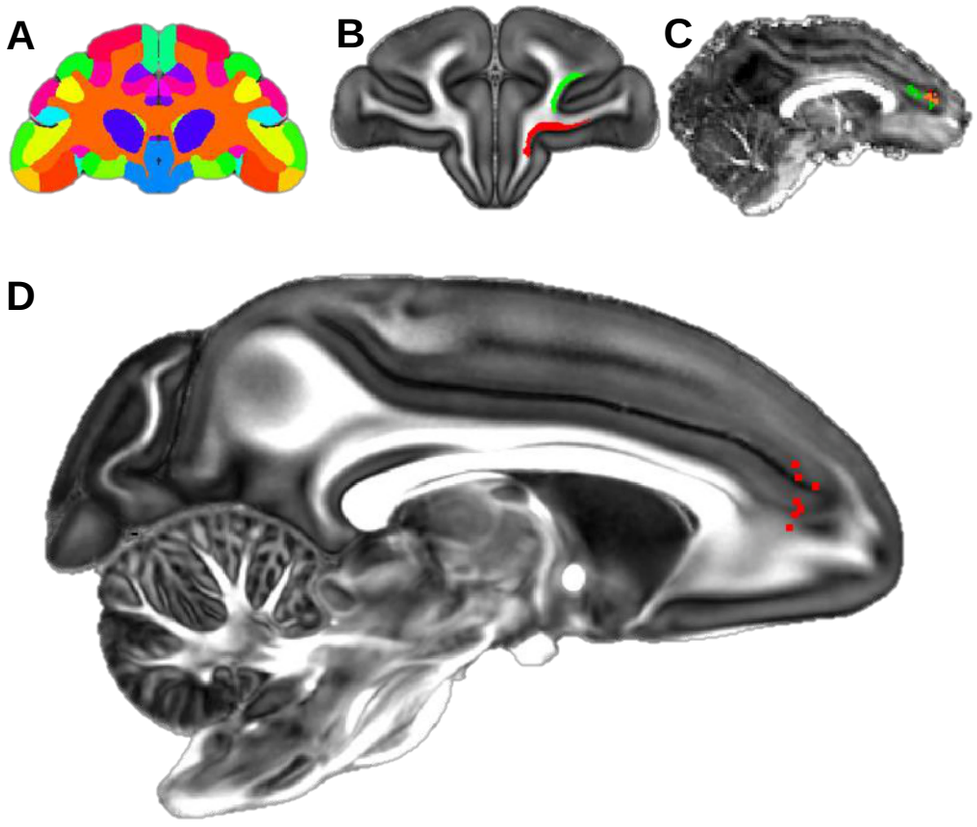
A
B
C
D

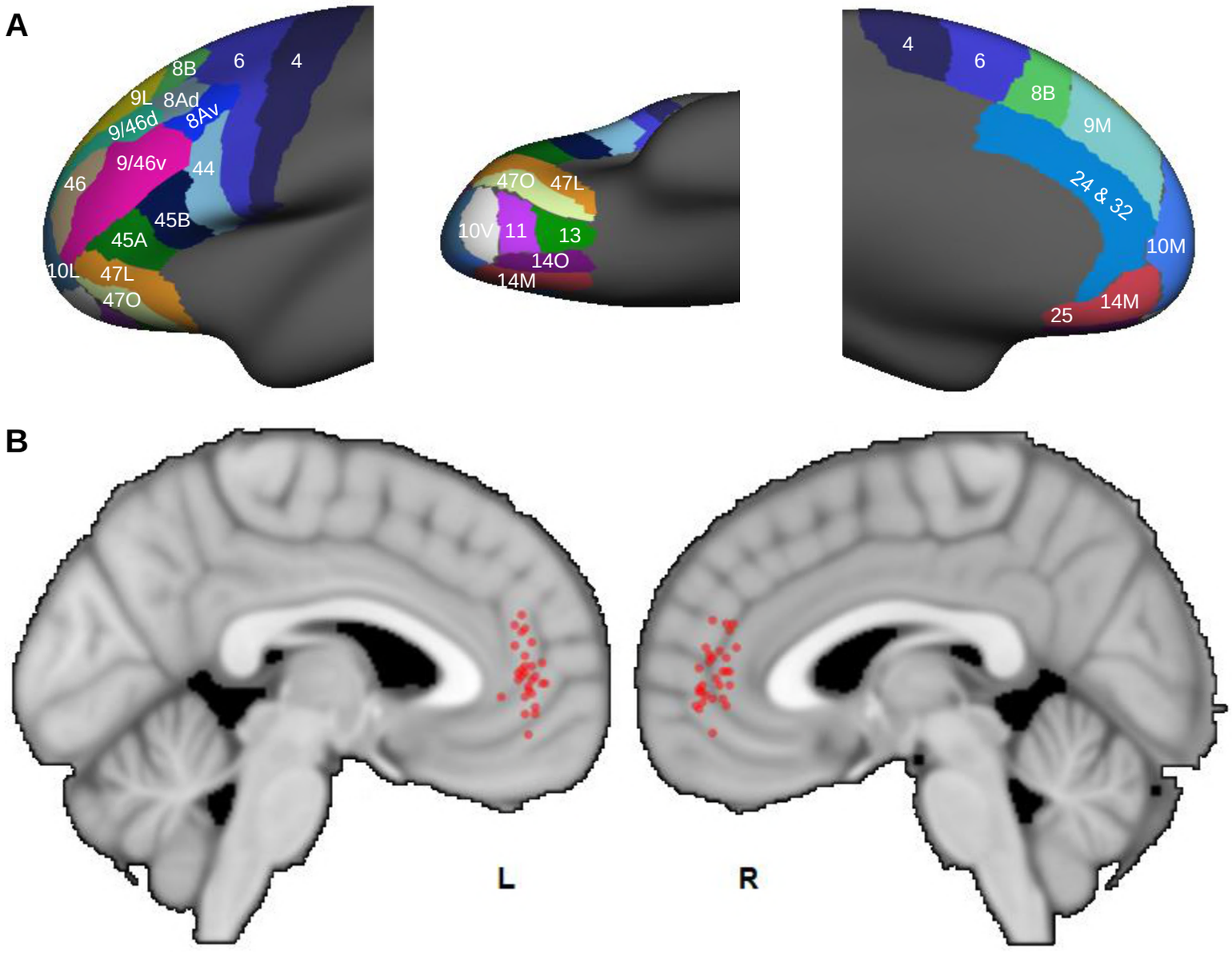
A
8B
6
4
9L
8Ad
8Av
9/46d
9/46v
44
46
45B
45A
10L
47L
47O
47O
47L
10V
11
13
14O
14M
4
6
8B
9M
24 & 32
10M
14M
25
B
L
R

Figure S1

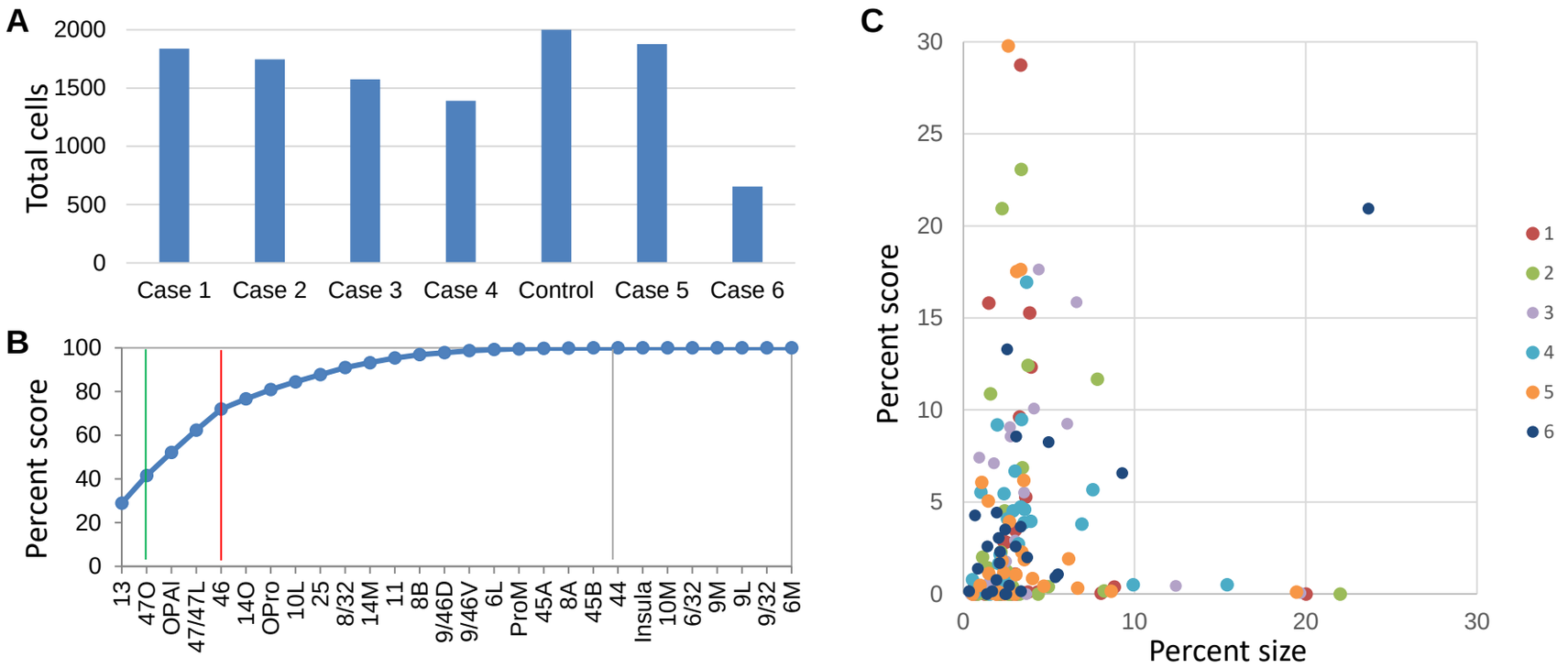
A
Total cells
2000
1500
1000
500
0
Case 1
Case 2
Case 3
Case 4
Control
Case 5
Case 6
B
Percent score
100
80
60
40
20
0
13
47O
OPAI
47/47L
46
14O
OPro
10L
25
8/32
14M
11
8B
9/46D
9/46V
6L
ProM
45A
8A
45B
44
Insula
10M
6/32
9M
9L
9/32
6M
C
Percent score
30
25
20
15
10
5
0
0
10
20
30
Percent size
1
2
3
4
5
6

Figure S2

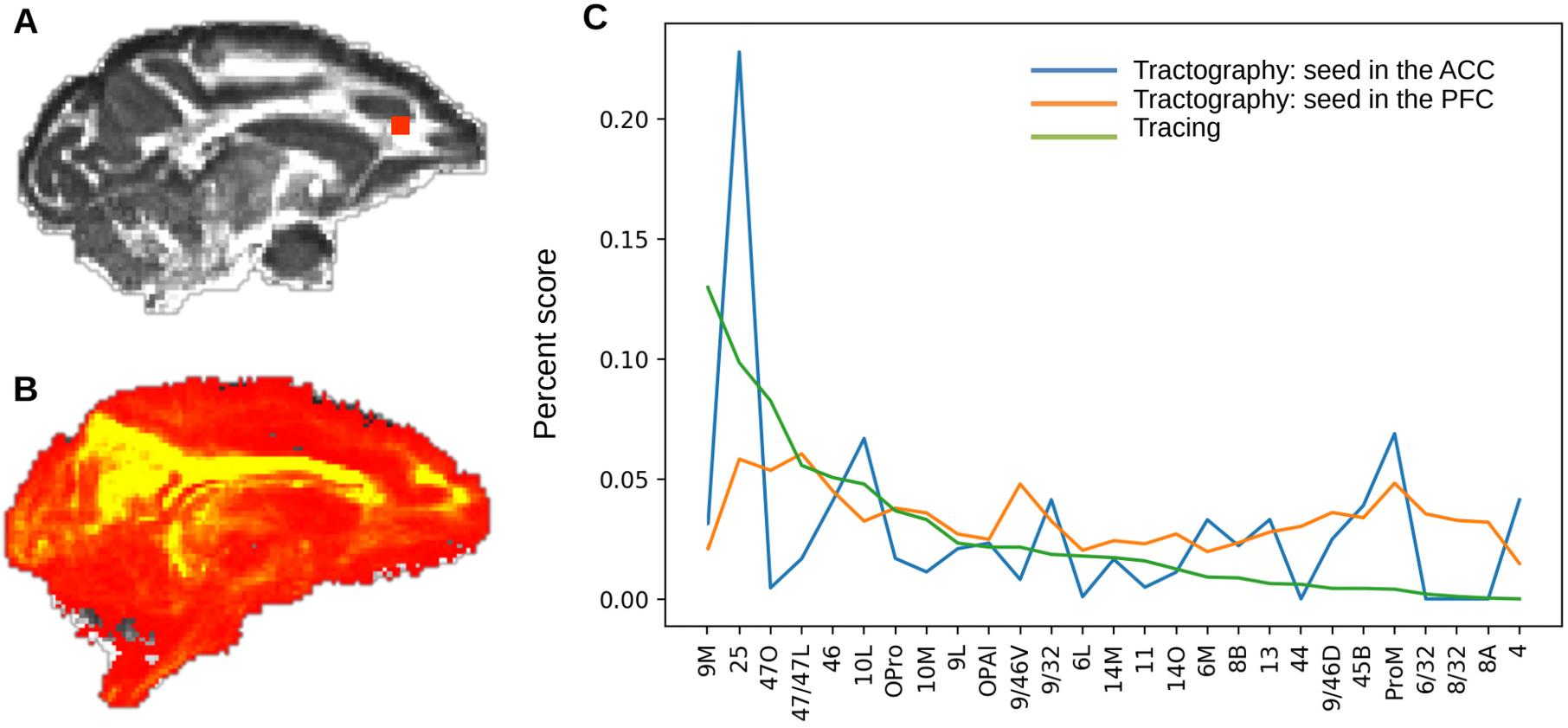
A
B
C
Tractography: seed in the ACC
Tractography: seed in the PFC
Tracing
Percent score
0.20
0.15
0.10
0.05
0.00
9M
25
47O
47/47L
46
10L
OPro
10M
9L
OPAI
9/46V
9/32
6L
14M
11
14O
6M
8B
13
44
9/46D
45B
ProM
6/32
8/32
8A
4